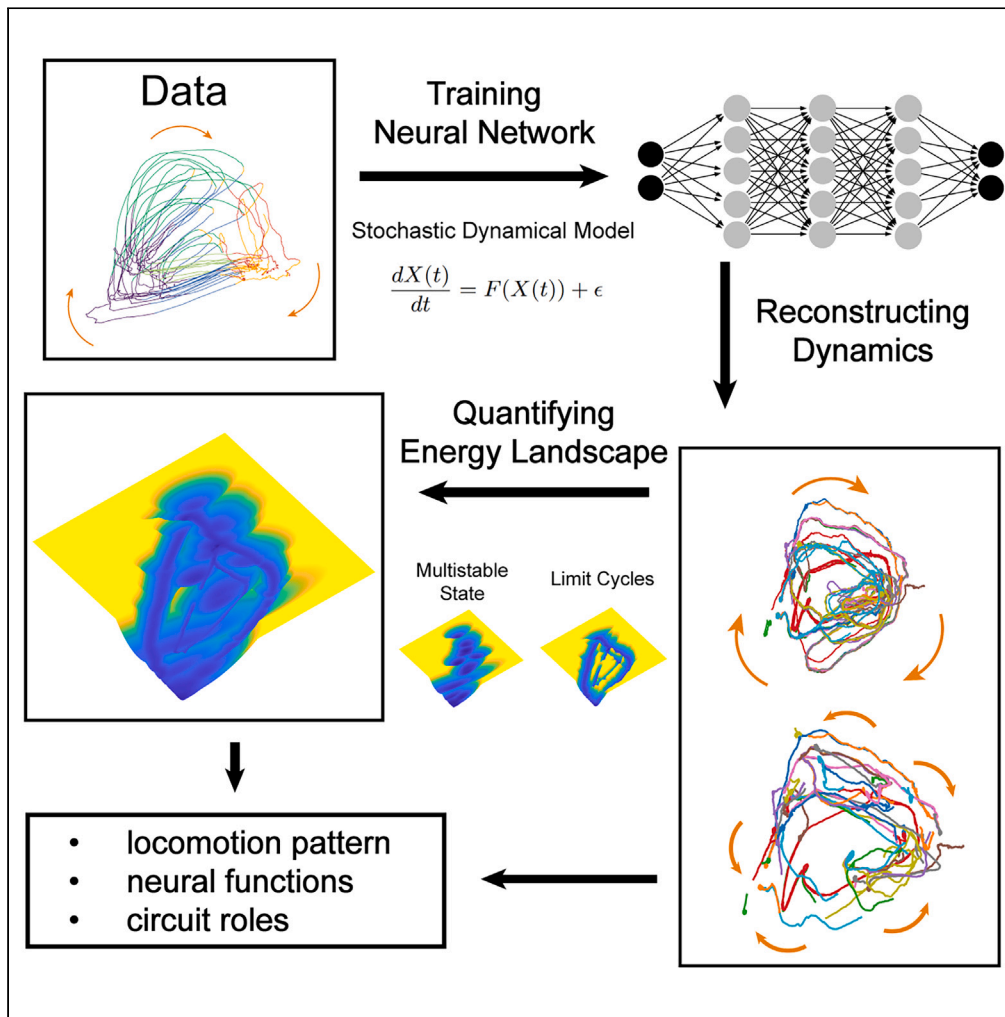


Article

# Revealing neural dynamical structure of *C. elegans* with deep learning



Ruisong Zhou,  
Yuguo Yu, Chunhe  
Li

chunheli@fudan.edu.cn

**Highlights**

Reconstructing the neural dynamics for the locomotion of *C. elegans* by a DNN model

Identifying two limit cycles essential to the pirouette behaviors

Quantified energy landscapes from DNN model explain the switching strategy

Model provides testable predictions on neural functions and circuit roles



## Article

Revealing neural dynamical structure of *C. elegans* with deep learningRuisong Zhou,<sup>1</sup> Yuguo Yu,<sup>2,3</sup> and Chunhe Li<sup>1,4,5,\*</sup>

## SUMMARY

***Caenorhabditis elegans* serves as a common model for investigating neural dynamics and functions of biological neural networks. Data-driven approaches have been employed in reconstructing neural dynamics. However, challenges remain regarding the curse of high-dimensionality and stochasticity in realistic systems. In this study, we develop a deep neural network (DNN) approach to reconstruct the neural dynamics of *C. elegans* and study neural mechanisms for locomotion. Our model identifies two limit cycles in the neural activity space: one underpins basic pirouette behavior, essential for navigation, and the other introduces extra  $\Omega$  turns. The combination of two limit cycles elucidates predominant locomotion patterns in neural imaging data. The corresponding energy landscape explains the switching strategies between two limit cycles, quantitatively, and provides testable predictions on neural functions and circuit roles. Our work provides a general approach to study neural dynamics by combining imaging data and stochastic modeling.**

## INTRODUCTION

*Caenorhabditis elegans* (*C. elegans*) represents one of the animals with the simplest neural system and is widely used to investigate neural dynamics. The neural system of *C. elegans* consists of 302 neurons with a known connectome, and recent advancements in neuronal imaging have yielded substantial imaging (neural activity) data, which lays the foundation for exploiting data to investigate the neural dynamical mechanisms of *C. elegans*. Investigating the underlying neural dynamics of *C. elegans* is instrumental in unraveling the broader workings of natural neural networks. Thus, it becomes essential to reconstruct the neural networks of *C. elegans* and corresponding dynamical models from neural activity data. Numerous computation models are developed to infer the neural dynamical structure of *C. elegans*. Some of these models are grounded in the neural connectivity,<sup>1–4</sup> while the others are solely data-driven.<sup>5,6</sup> Connectivity-based models have the potential to investigate the function of neural circuits and directly reveal the relationship between the neural dynamics and the network structure.<sup>3</sup> However, the nonlinear structure results in the sensitivity for the connectivity coefficients and synaptic polarity.<sup>5,7,8</sup> The constrained available experimental measurements pose challenges for accurate simulations.

The data-driven approaches provide us a promising method for reconstructing the dynamics solely from the imaging data and enabling reliable simulation. Nevertheless, practical challenges persist. The complex, nonlinear dynamics need to be reconstructed from vast datasets, imposing substantial computational costs. The curse of dimensionality brings challenges to reconstructing the dynamics through traditional ways. To overcome these challenges, some data-driven methods confine the model to a few neurons or principal components (less than five),<sup>3,6</sup> or impose constraints on dynamic forms.<sup>5</sup> Introducing a higher dimensional model remains challenging. On the other hand, based on the previous dataset and methods, few of the previous computation models give predictions for both neural activity data and locomotion behaviors. Previous works on computation modeling usually either simplify the behaviors into binary “Forward” and “Backward” states,<sup>1</sup> or introduce several behaviors into the model but only focus primarily on the dynamics within these two states,<sup>5,6</sup> almost omitting the turns. Additionally, the dynamical structure governing the stable states and the periodic oscillation remains unclear, and the underlying mechanisms guiding state transitions are largely unexplored within these computational frameworks. Difficulties persist in using the computation models to reveal dynamics governing the transition of behavior states and the switching between locomotion strategies. Furthermore, the impact of perturbing certain neurons on motor behaviors is challenging to predict within existing computational frameworks.

Deep learning presents an attractive solution for decoding neural activity due to its ability to effectively learn complicated, nonlinear transformations from data.<sup>9–11</sup> Its applications extend across various domains, including investigating neural dynamics, gene dynamics, cell movement and properties of pharmacogenomics.<sup>12–16</sup> The utility of deep learning becomes particularly evident when dealing with the complexities

<sup>1</sup>School of Mathematical Sciences and Shanghai Center for Mathematical Sciences, Fudan University, Shanghai 200433, China

<sup>2</sup>Research Institute of Intelligent and Complex Systems, State Key Laboratory of Medical Neurobiology, MOE Frontiers Center for Brain Science, and Institute of Science and Technology for Brain-Inspired Intelligence, Fudan University, Shanghai 200433, China

<sup>3</sup>Shanghai Artificial Intelligence Laboratory, Shanghai 200232, China

<sup>4</sup>Institute of Science and Technology for Brain-Inspired Intelligence and MOE Frontiers Center for Brain Science, Fudan University, Shanghai 200433, China

<sup>5</sup>Lead contact

\*Correspondence: [chunheli@fudan.edu.cn](mailto:chunheli@fudan.edu.cn)

<https://doi.org/10.1016/j.isci.2024.109759>



arising from high-dimensional data and complex forms of dynamic forces. Inspired by previous studies on deep-learning neural networks (DNN) and neural dynamics modeling,<sup>17–19</sup> we seek to perform DNN to reconstruct the neural network of *C. elegans*. Kato et al. proposed  $Ca^{2+}$  imaging to record the neural activity data of *C. elegans* and their research also provides the corresponding behavior state series.<sup>20</sup> This dataset has been instrumental in investigating the dynamics behind the pirouette behavior,<sup>5,6</sup> which is central to the navigation for *C. elegans*.<sup>16,21–24</sup> We aim to reconstruct the DNN model from this dataset, and we also propose two methods for explaining the locomotion behaviors corresponding to the simulations. These approaches allow us to provide both neural activity and locomotion states, and help us investigate the mechanism of behavior transitions in the computation model. Furthermore, after introducing the inhibition force in the DNN model, it becomes possible to predict the change of locomotion for *C. elegans* after making perturbations to certain neurons.

The energy landscape approach serves as a valuable tool for examining stochastic dynamics in biological networks.<sup>18,25–29</sup> It has been employed to uncover global properties of the dynamics of complex networks. Inspired by the previous studies on the energy landscape, we introduce the Gaussian noise to our DNN model to study the stochasticity and calculate the energy landscape of the neural system. The energy landscape provides us with ways to reveal the switching strategies from a global perspective.

Our model yields several noteworthy findings. Firstly, The DNN model for *C. elegans* effectively captures the essential features of neural dynamics and exhibits strong performance within a short time. Notably, it identifies two limit cycles in the neural activity space. Second, upon further analysis of locomotion behaviors, we uncovered that one of these limit cycles underlies the fundamental pirouette behavior, while the other is associated with the extra  $\Omega$  turns in the pirouette behavior. Intriguingly, the occurrence of the second-type limit cycle within a pirouette behavior aligns with a geometric distribution, which means the probability decreases exponentially as the increase of occurrences. This intriguing discovery, along with the interplay between the two types of limit cycles, accounts for a significant portion of the behavior sequences observed in brain-wide calcium imaging data. Thirdly, we observe that the model with middle-level noise provides the best fit for *C. elegans* locomotion behaviors. Moreover, the energy landscape of *C. elegans* neural dynamics unveils a structured interplay of attractors and limit cycles, which explains the geometric distribution observed. This discovery provides valuable insights into the mechanisms underlying the switching of locomotion strategies. Finally, our approach, incorporating both the energy landscape and neural inhibition in the DNN model, provides the confirmations and predictions for the functions of key neurons and circuits for locomotion.

Our work proposes a data-driven approach to infer the dynamical structure of *C. elegans* and introduces two methods for explaining the locomotion of the simulation (Figure 1). The computation model offers valuable insights into the transition mechanisms for behaviors within pirouette strategies and the roles of neurons for locomotion.

## RESULTS

### DNN model for *C. elegans* captures the key information of neural dynamics

In prior experiments, approximately 100 neurons in the head ganglia are recorded simultaneously in each of five animals immobilized in a microfluidic chamber.<sup>20</sup> Among the 21 consistently and unequivocally identified neurons in each individual, we selected 14 key neurons of *C. elegans*, including both the sensory interneurons and motor neurons (Figures S1 and S2). Kato et al.<sup>20</sup> employed imaging to observe a limited subset of neurons in freely moving *C. elegans*, confirming the close correlation between the activation of certain individual neurons and locomotion parameters. This leads to the interpretation of neural activity in immobilized animals as motor commands indicative of locomotor behaviors. Kato et al. provide the corresponding time series of locomotor behavior in immobilized animals, which is grounded in the activation of neurons. Several previous studies exploring the neural dynamics of *C. elegans* locomotion are also grounded in the neural activity data and behavioral states provided by Kato et al..<sup>2,5,6,20</sup> Therefore, we seek to develop a model to reconstruct the neuron dynamics of *C. elegans* and investigate the underlying dynamical structure governing the locomotion of *C. elegans* based on these neural activity data.

Before introducing our model, we conducted an initial analysis of motor command transitions using the imaging dataset. We commenced this analysis by calculating the transition probabilities between different behavioral states using the time series data of *C. elegans* from Kato's imaging dataset.<sup>20</sup> Within this dataset, behaviors are categorized into six states: Forward, Slow, Reverse, Sustain reverse, Dorsal turn and Ventral turn. Forward and Sustain Reverse represent smooth forward and backward locomotion. The Slow states signify a decrease in forward speed, whereas Reverse indicates an increase in backward speed. Dorsal turn and Ventral turn represent turns in the respective directions. Importantly, distinct trajectories in the Slow state imply the need for further division into transient Slow1 and sustained Slow2 states (see more details in STAR Methods). Subsequently, we constructed a state transition diagram (Figure 3A) to intuitively comprehend locomotion patterns, with arrow thickness representing transition probability magnitudes. According to the diagram, the Forward state transitions exclusively to Slow or Reverse states. The Reverse state precedes two types of turns before returning to the Forward or Reverse states through the Slow state. Notably, the diagram highlights two primary cycles: "Forward  $\rightarrow$  Slow  $\rightarrow$  Reverse  $\rightarrow$  Sustain reverse  $\rightarrow$  Dorsal/Ventral turns  $\rightarrow$  Forward" and "Sustain reverse  $\rightarrow$  Dorsal/Ventral turns  $\rightarrow$  Slow  $\rightarrow$  Reverse  $\rightarrow$  Sustain reverse". These two cycles are specifically highlighted in Figure 3B.

We proceed by introducing our deep-learning neural network (DNN) approaches to reconstruct the neural dynamics of *C. elegans*. Previous studies have generally characterized the neural dynamics as a stochastic system<sup>19</sup>:

$$\frac{dX}{dt} = F(X) + \epsilon, \quad (\text{Equation 1})$$

where  $F$  represents the deterministic driving force and  $\epsilon$  signifies noise, which we assume as Gaussian white noise. We employ a three-layer feedforward neural network in our approach to reconstruct the deterministic driving force. The network is trained (Figure S3A) on the imaging

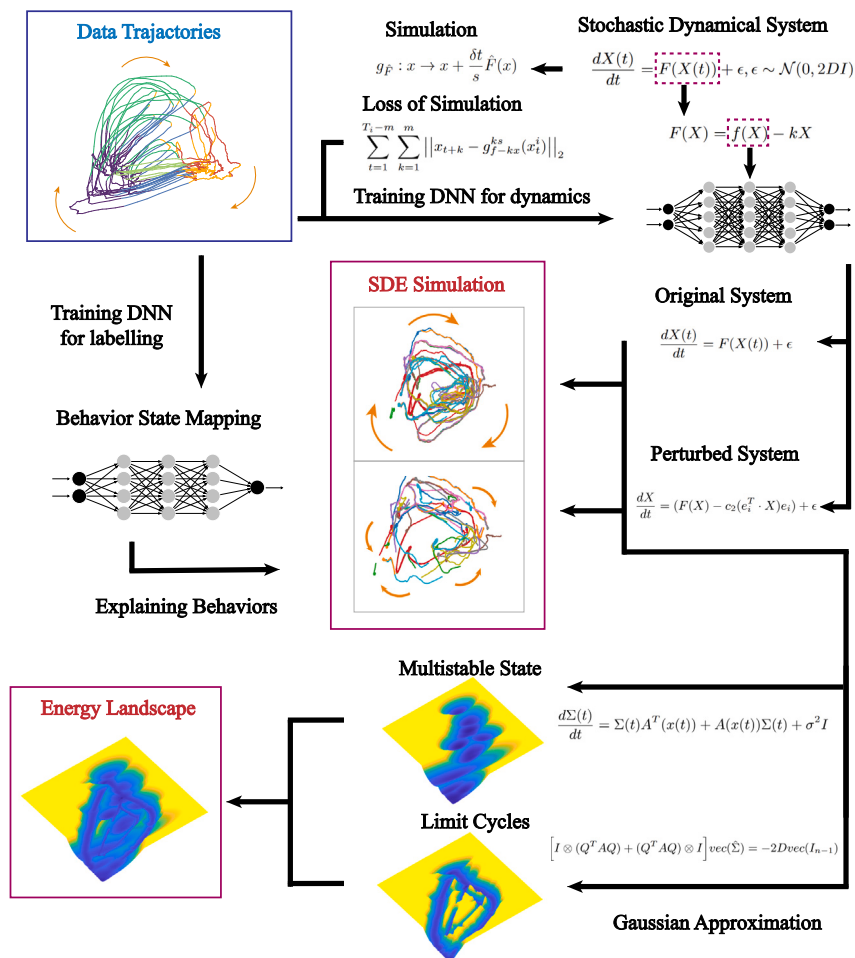


**Figure 1. Data-driven approach for constructing energy landscape**

The data trajectories are used to train the Deep-learning Neural Network for dynamics and reconstruct the neural dynamics. The reconstructed dynamics correspond to the deterministic force in the dynamical system. The trained DNN is used to approximate one part of the dynamics while the other part is  $-kX$ . Using the trained DNN, we get the original system. Adding the “inhibition force” (see details in STAR Methods), we get the perturbed system. The SDE simulations of the two dynamical systems give the prediction of neural activity. The behavior labels of data trajectories in the dataset are used to train the DNN for behaviors and this trained DNN helps to explain the behavior states in the SDE simulation. Using the previous approaches for multistable states and our new methods for limit cycles, we can quantify the energy landscape of two types of systems. The energy landscape further helps us to investigate the underlying dynamical mechanisms.

dataset<sup>20</sup> using a curve-fitting method, minimizing deviations between the data and the simulations by network (see more details in STAR Methods). Utilizing this trained neural network, we are able to conduct simulations for the neural activity under different noise conditions. In our model, we specifically incorporate Gaussian white noise with varying levels, represented by different covariances. Previous works showed neural activity evolves on a low-dimensional manifold,<sup>5,20</sup> which is reproduced by projecting imaging data (Figure 2A, gray lines). Notably, our simulations, starting from data points, align with this manifold under various noise levels (Figure 2A). This observation indicates that the manifold arises from the underlying dynamical structure, which is captured by our models. Besides, we observe that the simulation trajectories in time series exhibit deviations from the data trajectories, but after a time shift they align closely (Figure S3B corresponding to the left panel of Figure 5C and S3C corresponding to the right panel of Figure 3E), and in these cases the normalized mean squared error (NSME)  $\frac{\|x_{\text{simu}} - x_{\text{data}}\|_2}{\|x_{\text{data}}\|_2}$  reaches the level around 5%. Importantly, after this time shift, it’s observed that both trajectories originate from the same stable state. Therefore, the deviations between simulation and data trajectories may primarily arise from the different resting times or different evolution types from the stable states. A comprehensive analysis of the data trajectories validates this observation, uncovering significant deviations between two data trajectories that commence from the same stable state (Figure S4).

In summary, our model effectively captures the primary features of the dynamical structure of *C. elegans* and facilitates reliable predictions for neural activity. To explain the locomotion behaviors for our simulations, we need a map function to correlate the neural activity series to corresponding behavior labels. Since only a few motor neurons are selected in our model, it’s hard to use their activations as indicators for the

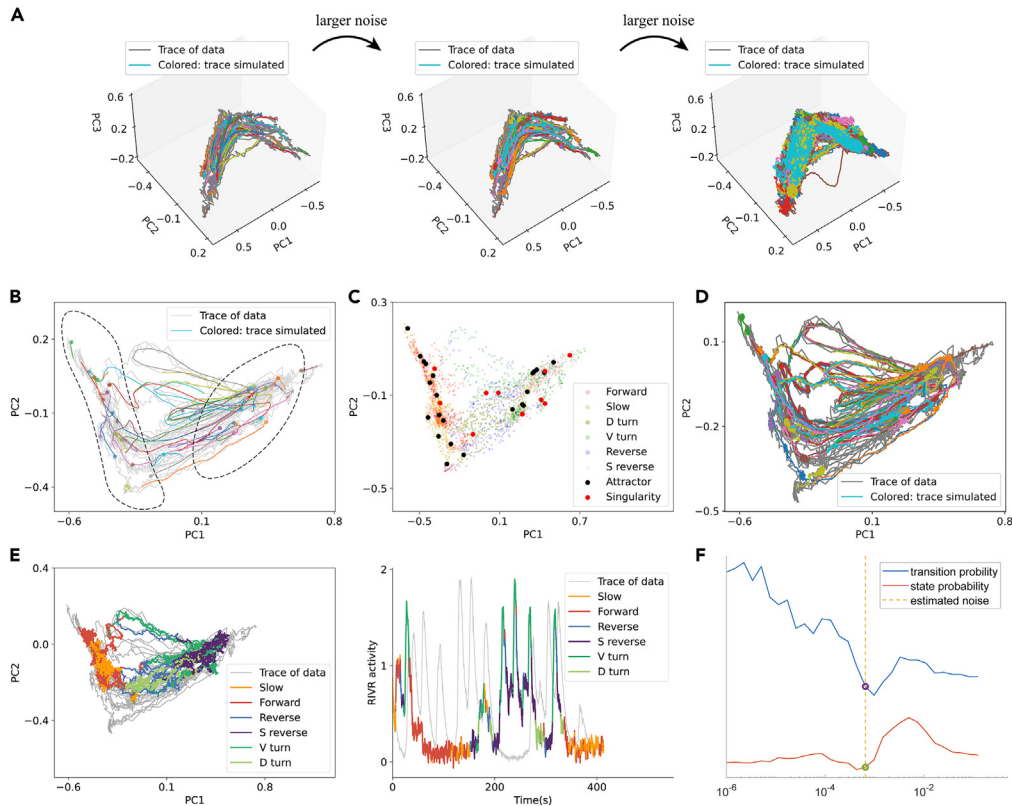


**Figure 2. The Gaussian noise is a critical factor influencing the choice of strategy**

(A) The projection of simulation traces under different noise levels (no noise on the left, middle noise in the middle, and large noise on the right) onto the first three principal components. These traces are color-coded for comparison with gray traces representing experimental data. All of them conform to a low-dimensional manifold.

(B) Projections of simulated trajectories onto the first two principal components. The simulations are performed without noise with the start points randomly selected from the dataset (see more details in STAR Methods). These trajectories ultimately converge to some stationary points which are circled with black dotted lines.

(C) All the stationary points, with attractors marked in black and others in red. All attractors belong to the Forward and Sustain reverse states.

(D) Projections of simulated traces under middle noise onto the first two principal components.

(E) A simulated trace under large noise. Its projection onto the first two principal components (left panel) and the neural activity of neuron RIVR (right panel) are shown. Under the large noise, neural activity oscillates rapidly and randomly between various cycles, traversing a substantial portion of the manifold.

(F) KL divergence of state probability (red) and state transition probability (blue) between the data and simulations under different noise levels. The estimated noise level is estimated from the dataset using Maximum Likelihood Estimation (MLE) (see more details in STAR Methods).

complicated movement states. Therefore, we introduce a clustering method and a DNN method (see more details in STAR Methods) to learn the map from the dataset. These methods help to assign behavior states to each point in our simulations. With these assigned states, we can effectively describe the locomotion behaviors exhibited in these simulation trajectories. Within our implementation, both approaches yield remarkably similar time series of behavior states. Consequently, in the following sections of this article, we consistently refer to the behavior series derived through the DNN method. These corresponding behavior series, across most noise levels in our simulations, align with the previously mentioned pattern of motor command alterations in the dataset. This discovery reinforces the notion that our model adeptly captures the fundamental behavioral mechanisms of *C. elegans*.

### Model with middle level noise better explains behaviors of locomotion

To study the effects of stochasticity on the model, we have added the noise with different noise levels to the DNN model. Additionally, we determine the estimated noise level from the dataset using Maximum Likelihood Estimation (MLE). Further details are available in the STAR Methods. To investigate the underlying dynamical structure and assess the noise impact on *C. elegans* locomotion, we examine three specific cases: no noise, middle noise (estimated from the data), and large noise. Confirming our previous observation, all these trajectories are restricted to the low-dimensional manifold (Figure 2A). Under no noise, all the trajectories converge to specific stationary points where the deterministic driving force vanishes (Figure 2B). Further analysis of these points identifies the attractors (Figure 2C) in the neural dynamical

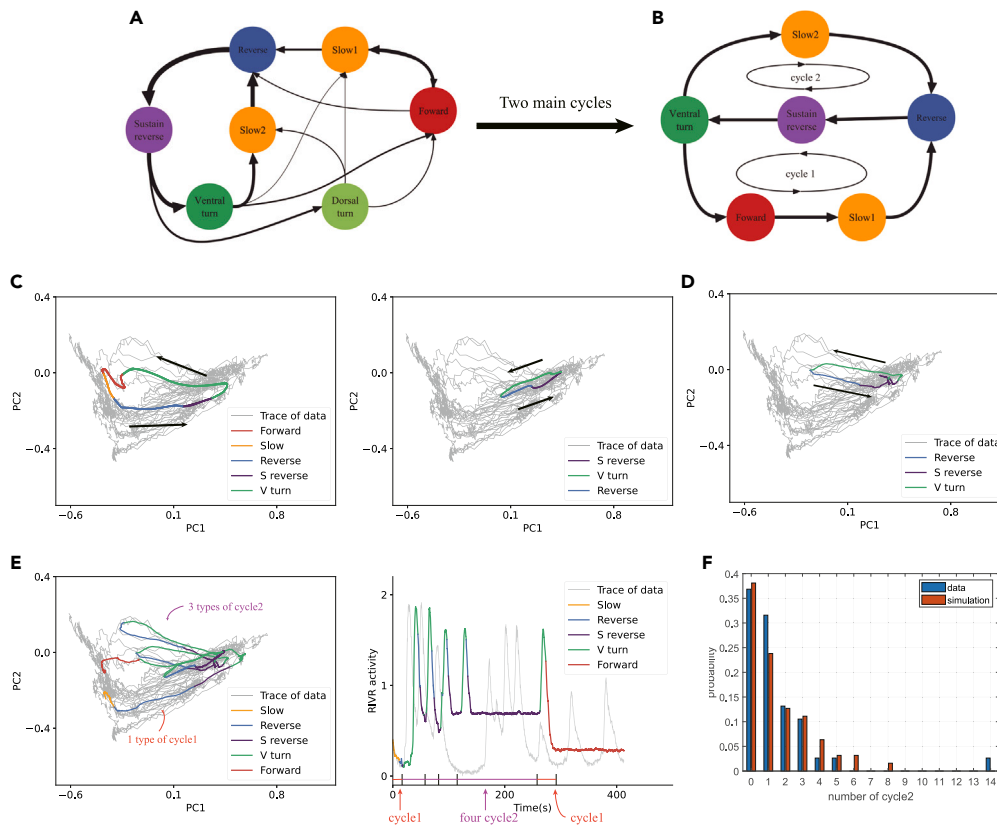


**Figure 3. Two limit cycles identified by the DNN model governing the underlying mechanisms for locomotion**

(A) The state transition diagram derived from the experimental dataset, where the thickness of the arrows is positively correlated to the probability of transition. (B) The transition diagram featuring the two primary cycles. The two cycles in the transition diagram correspond to the two limit cycles in the neural activity space. (C) The representation of two limit cycles when projected onto the first two principal components. Cycle 1 (left panel) aligns with the fundamental sequence in the pirouette strategy, while Cycle 2 (right panel) represents the extra  $\Omega$  turns. The Slow states with 2~3 frame duration in Cycle 2 are overshadowed by other states. (D) A cyclic trajectory lying in the orbit of Cycle 2. These cyclic traces add diversity to the forms of  $\Omega$  turn. (E) A representative simulation trace projected onto the first two principal components (left) and neuron RVR (right). This trajectory depicts four Cycle 2 in a pirouette behavior, illustrating the variation of the pirouette behaviors. By applying an appropriate shift, the simulated trace closely matches the data trace (see details in Figure S3C). (F) The distribution of the occurrences of Cycle 2 instances within a pirouette series (a series from Forward states to Forward states), i.e., the number of Cycle 2 between two Cycle 1. This distribution aligns with the geometric distribution with expectation 1.5(data)/1.56(simulation) ( $p$ -value = 0.0008/0.0182, Goodness of fit test).

system of *C. elegans* (see more details in STAR Methods). We find that there are a significant number of attractors in the activity space and all these attractors correspond to the Forward and Sustain reverse states. This observation implies that these two sustained locomotion behaviors correspond to diverse stable states, each associated with specific attractors. Different stable states indicate different thresholds to transition and different transition patterns. To further investigate other dynamical structures, we proceed by increasing the noise level. At the middle noise level, the trajectories evolve from fragmented segments (Figure 2B) to cyclic patterns (Figure 2D). Analyzing these trajectories, our model identifies two distinct limit cycles (Figure 3C solid lines). With the large noise, neural activity undergoes rapid and random oscillations between different cycles, covering a significant portion of the manifold. Ultimately, it approximates a random walk in the manifold (Figure 2E).

Model with no noise exhibits consistent behaviors, while model with large noise lacks repetitive behavior series and exhibits inaccurate state transitions (Figure 2E) compared to the transition patterns from data (Figure 3A). Consequently, neither of these extremes corresponds to the observed behavior patterns of *C. elegans*. For a quantitative evaluation of the consistency between simulations and actual behavior, we calculate the Kullback-Leibler (KL) divergence for both state probability and state transition probability under different noise levels in comparison to the imaging dataset (Figure 2F). Intriguingly, it indicates that both KL-divergence optimizes at middle noise levels and the estimated noise level is in close proximity to these two optimal points. This observation emphasizes the substantial impact of noise levels on the locomotion patterns of *C. elegans*, highlighting that the model with the middle noise level provides a more accurate explanation for its locomotion behaviors. Significantly, it also suggests that the estimated noise level serves as a suitable approximation for the optimal noise level.

## Two limit cycles reveal the underlying mechanisms of the pirouette strategy

In the neural activity space, our DNN model has identified two distinct limit cycles (Figure 3C solid lines), denoted as Cycle 1 (left panel of Figure 3C) and Cycle 2 (right panel of Figure 3C). Correspondingly, the behavior series illustrates the locomotion of *C. elegans* within these two cycles, remarkably mirroring the two primary cycles identified in the state transition diagram derived from the data (Figures 3A and 3B). During Cycle 1, the locomotion sequence commences with forward movement and deceleration, followed by a reverse locomotion phase and sustained backward motion. Subsequently, a ventral turn occurs, leading to a subsequent switch back to forward locomotion. In Cycle 2, the locomotion begins with sustained backward movement. It then transitions into a ventral turn, which is then followed by a reversal phase to resume sustained backward locomotion. These two behavior series have also been addressed in some previous studies. Cycle 1 is denoted as basic pirouette behaviors<sup>2</sup> and type-II transitions,<sup>3</sup> while Cycle 2 is simply referred to as  $\Omega$  turns.<sup>2</sup> Moreover, these two behavioral sequences align with the two distinct branches of the low-dimensional manifold.<sup>5</sup> Therefore, it is convincing that the two identified limit cycles constitute the fundamental dynamical structure governing the pirouette strategy.

Further analysis of the behavior series in the dataset reveals that flexible locomotion primarily manifests as combinations of the two typical behavior sequences mentioned earlier. We systematically enumerate all behavior sequences starting in the Forward state and ending in the Forward state. By mixing up two types of turns, and excluding all sequences of Cycle 2, the remaining sequences can be classified into two types. The first corresponds to the behavior sequences of Cycle 1, while the second involves a series of oscillations between the Forward and Slow1 states. Furthermore, the majority of behavior series in the dataset can be explained by the combination of the behavior series of the two identified limit cycles. Our simulations with middle and large noise levels validate these findings (Figure 3E). Thus, the mechanisms of locomotion are likely rooted in the intricate interaction between these two limit cycles.

To characterize the interaction between the two limit cycles, we analyze the instances of Cycle 2 within a “Forward  $\rightarrow$  Sustain reverse  $\rightarrow$  Forward” sequence. The count (Figure 3F) closely conforms to a geometric distribution ( $p$ -value = 0.0008 and expectation 1.5 for data,  $p$ -value = 0.0182 and expectation 1.5 for simulation, Goodness of fit test). The geometric distribution indicates that the probabilities of entering Cycle 1 and Cycle 2 at the intersection area are constant, i.e., independent of previous trajectories. Each “Forward  $\rightarrow$  Sustain reverse  $\rightarrow$  Forward” sequence is constituted by a Cycle 1 instance with several “Cycle 2 decisions” in the intersection area. This sequence corresponds to pirouette behaviors with several  $\Omega$  turns; therefore, we term it the pirouette series. The intersection area plays a special role in choosing which limit cycle to enter, so we refer to it as the transition area (Figures 3E, 4A, and 4D).

We aim to investigate additional properties emerging from the dynamical structure within the transition area. Several attractors in the activity space have been identified, and notably, an attractor in the Sustain Reverse state is situated within the intersection area of two limit cycles (Figure 4D). This attractor serves as the preparation point for making decisions for movement. Additionally, we observe significant variation in the stability of the two limit cycles. In our simulations with a smaller noise level, trajectories starting from Cycle 1 exhibit almost no departures within the span of 10 periods (Figure 5C), while those starting from Cycle 2 frequently deviate after 1 to 4 periods (Figure 5D). Since the deviations mainly occur in the attractor of the transition area and the main choices at this attractor are entering two limit cycles (Figure 4D), our observation indicates that within the attractor, the probability of entering a new Cycle 1 is higher than that of entering a new Cycle 2 under small noise level. Furthermore, this observation also reveals that under the small noise level, the stability of Cycle 1 is higher than Cycle 2.

Now we aim to use the corresponding behavior series to explain the intricate interaction between two limit cycles. Both limit cycles contribute to pirouette behaviors: Cycle 1 represents the simplest pirouette behavior with only one period of  $\Omega$  turn, while Cycle 2 can be characterized as a  $\Omega$  turn. Given that only Cycle 1 passes through the Forward states, it plays a crucial role in initiating the pirouette, thereby laying the foundation for basic pirouette strategies. Consequently, Cycle 2 can be considered as  $\Omega$  turns inserted into the pirouette behavior series. Specifically, the last  $\Omega$  turn is attributed to Cycle 1, while the others originate from Cycle 2, indicating that Cycle 2 contributes to the additional  $\Omega$  turns in pirouette behaviors. In summary, Cycle 2 introduces diversity to pirouette behavior, while Cycle 1 plays the role of initiation.

## Energy landscape and probability flux of neural dynamics of *C. elegans*

While we delved into the dynamical structure that governs the locomotion patterns of *C. elegans*, understanding how these patterns emerge from this structure still eludes us. To delve deeper into these mechanisms, a comprehensive view of *C. elegans* dynamics is essential. The energy landscape, known for its efficacy, provides this global perspective. The energy landscape (also referred to as the potential landscape) has found widespread application in studying stochastic dynamics across various biological systems.<sup>18,19,26–30</sup> In this approach, the dynamics of the system are modeled by a deterministic driving force  $F$  with white noise  $\epsilon$  (Equation 1).

For simplicity, we assume the white noise here is independent Gaussian noise, that is  $\epsilon \sim N(0, \frac{D}{2}I)$ . Now the evolution of corresponding probabilities can be described by the Fokker-Planck equation:

$$\frac{dP}{dt} = -\nabla J(X, t), \quad (\text{Equation 2})$$

$$J(X, t) = F(X)P - D\nabla P.$$

By calculating the steady distribution  $P_{ss}$  which satisfies  $\frac{dP_{ss}}{dt} = 0$ , we can decompose the deterministic dynamic force into a conservative force and a flux

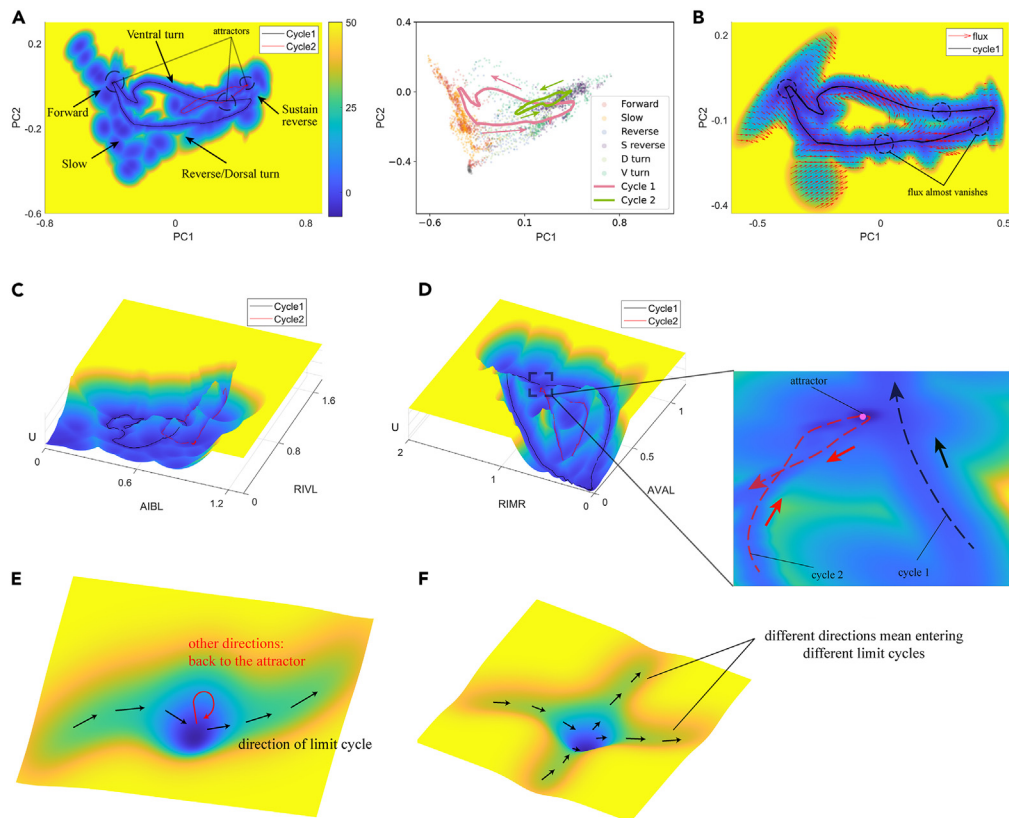


**Figure 4. Potential landscape provides valuable insights into the global properties of dynamical structure**

(A) The potential landscape (left) and two limit cycles with data points color-coded according to their behavior states (right). On the potential landscape the behavior states that each area corresponds to are labeled with arrows. Both landscapes are projected onto the first two principal components. Basins with attractors are distinctly separated along PC1, corresponding to the Forward and Sustain reverse states.

(B) The landscape and flux on the approximated surface of Cycle 1. The landscape prevents deviation from Cycle 1 while the flux promotes the revolving along Cycle 1. The vanishing of flux allows the freedom for diverse cyclic trajectories.

(C and D) The landscape projected onto the space of AIBL/RIVL or RIMR/AVAL activity, with two limit cycles highlighted. The transition area is highlighted to reveal the combined structure of attractor and limit cycles.

(E and F) The landscape structure in some simplified cases, including the cases with an isolated attractor in a single limit cycle (left) and with an isolated attractor in the intersection of two limit cycles (right).

$$F(X) = D \frac{\nabla P_{ss}(X)}{P_{ss}(X)} + \frac{J(X)}{P_{ss}(X)}. \quad (\text{Equation 3})$$

And the energy landscape is defined as  $U(X) = -\ln P_{ss}(X)$ .<sup>27,28,30</sup>

Within the neural dynamics of *C. elegans*, incorporating the noise level estimated from the data (see more details in [STAR Methods](#)), we can calculate the energy landscape of the neural system, in comparison with two limit cycles and data points (Figure 4A). This energy landscape unfolds a global perspective, enabling an exploration of the dynamical structure formed by attractors and the two limit cycles. Within the energy landscape, the attractors form two distinct basins separated along the first principal component, with the deepest three attractors aligning with the positions of the two limit cycles. These attractors collectively contribute to the stability of the sustained locomotion. Within the three attractors situated at the two limit cycles, the leftmost corresponds to the Forward state, while the others align with the Sustain Reverse. Their special locations indicate that these attractors take a higher potential for starting a pirouette while others not. Remarkably, the central attractor among these three aligns with the previously discussed transition points (the attractors in the transition area).

For a deeper exploration of the dynamical structure shaped by two limit cycles, we present the energy landscape from various perspectives (Figures 4C and 4D). Additionally, we overlay the flux onto the potential landscape (Figure 4B) within the least square surface of Cycle 1. In the energy landscape (Figure 4A), the two limit cycles partition the space into two branches, forming tube-like orbits for cyclic behaviors. The transition area is the sole region connecting the two branches. In the least square plane (Figure 4B), we observe the flux nearly vanishing in certain sections of the limit cycles, permitting diverse cyclic trajectories around the limit cycle. Indeed, we have observed various cyclic trajectories around Cycle 2 (Figure 3D). In other words, these trajectories deviate from the Cycle 2 but still maintain cycling in a neighborhood of Cycle

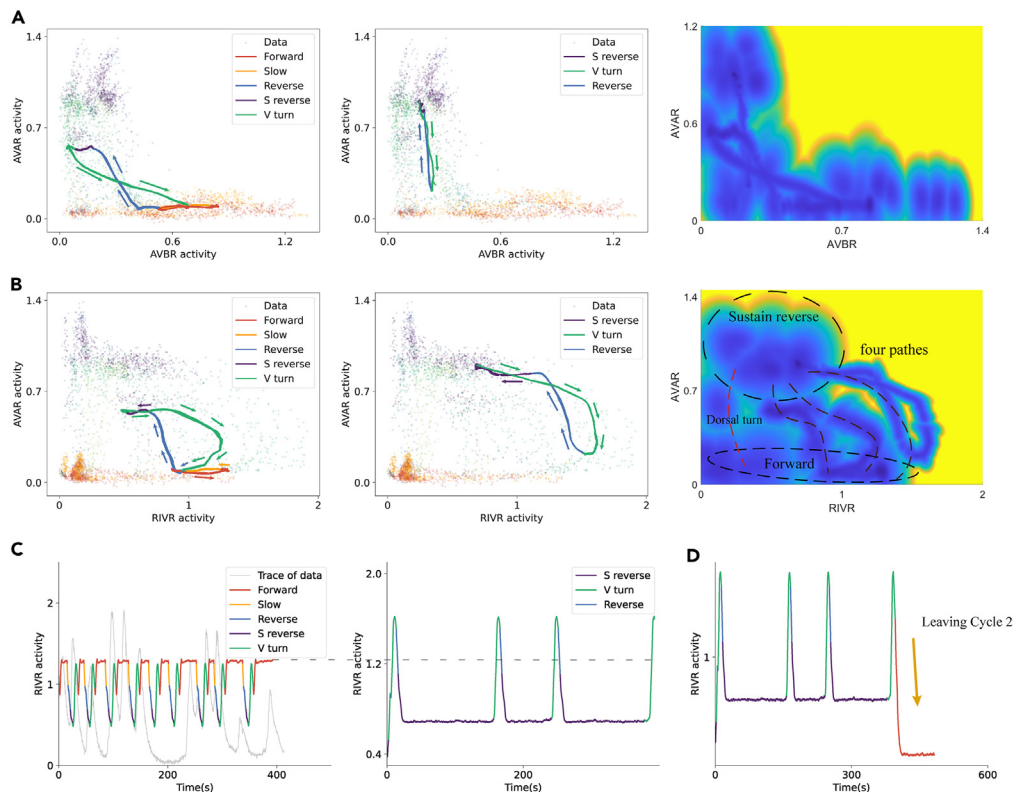


**Figure 5. The energy landscape with two limit cycles unveils the mechanisms of locomotion and confirms certain neural functions**

(A) The projection of two limit cycles and landscape onto the space of AVAR and AVBR. AVBR activity exhibits a negative correlation with AVAR activity in Cycle 1 (left panel), while it remains largely inactive in Cycle 2 (middle panel). The basins form an “L” shape (right panel).

(B) The projection of two limit cycles and landscape onto the space of RIVR and AVAR. In Cycle 1 (left panel), RIVR exhibits two peaks (Forward and Ventral turn) in each cycle, whereas in Cycle 2 (middle panel), it shows only one peak (Ventral turn). The landscape (right panel) identifies four paths connecting two stable states (Forward and Sustain reverse). The Forward state and Sustain reverse state are encircled and correspond to the red and purple areas in the left and middle panels. The trajectory that traverses the Dorsal turn state is highlighted in red, and the points within the Dorsal turn state are shaded in chartreuse in the left and middle panels.

(C) The activity of neuron RIVR in two limit cycles. Left panel: Cycle 1. Right panel: Cycle 2. It displays periodic variations within the two limit cycles, with significant fluctuations observed in the attractors at Forward state. The peaks of RIVR activity in Cycle 2 are much higher than peaks in Cycle 1.

(D) The activity of neuron RIVR for a simulated trajectory. This trajectory leaves Cycle 2 after 3 periods.

2. These cyclic trajectories add to the diversity of  $\Omega$  turns, corresponding to different lasting times and turning angles. The vanishing of flux in Cycle 1 forms another path connecting the Forward and Sustain Reverse state, by passing through the Dorsal turn states (Figure 5B, right panel). This dorsal-turn path, when accompanied with the two limit cycles, constitutes all the paths connecting the Forward and Sustain Reverse state (Figure 5B, right panel), exhibiting a noteworthy deviation in RIVR activity level. Consequently, in pirouette behaviors, RIVR activity emerges as a valuable indicator for distinguishing the current activity path and predicting the future locomotion of *C. elegans*. Importantly, the branch of Cycle 2 exhibits higher RIVR activity levels than the branch of Cycle 1 (Figure 5C). Given that Cycle 2 represents the additional  $\Omega$  turns, this observation may provide a dynamical explanation for the prior finding that higher RIVR activity aligns with frequent  $\Omega$  turns.<sup>31</sup>

To reveal how the transition patterns rise from the dynamical structure, we focus on the transition area, where an attractor is positioned, and two limit cycles intersect (Figure 4D). This attractor shapes steady-state probabilities with a Gaussian distribution,<sup>17,32</sup> creating a potential basin in the landscape. Simultaneously, limit cycles offer potential escape routes. Since the real structure in the transition area is complex, we initiate our exploration with simplified cases. Notably, the other two attractors in the limit cycles (Figure 4A) represent the simplest case where an isolated attractor is situated at a single limit cycle. Here, the sole escape route is along the direction of the limit cycle (Figure 4E). Attempts to escape in other directions lead to trajectory retracement and prolonged duration within the attractor. This finding elucidates the varied durations observed at the Forward state attractor in repeated traces (Figure 5C).

We now consider the cases featuring an isolated attractor at the intersection of two limit cycles. The two escape directions signify transitions into distinct limit cycles, whereas directions diverging from these lead back to the attractor (Figure 4F). Switching probabilities to different cycles are solely determined by the variance ratio of the Gaussian distribution along the directions of the two cycles. This implies that the probability is solely determined by the transient information at the attractor, irrespective of previous trajectories. Consequently, a

geometric distribution emerges for the number of one type of limit cycle between two with the other type. From this perspective, manipulating the covariance of the attractors can influence both the evolution of the system and the rates of the two limit cycles.

However, we observe that real cases in the transition area unfold with greater complexity. In such instances, the attractor is positioned at Cycle 2, while Cycle 1 merely intersects the neighborhood of the attractor (Figure 4D). This scenario bears resemblance to the earlier case under sufficient noise levels, yet an exceedingly small noise here may result in a decrease of the transitions. Consequently, under low noise levels, the divergence from Cycle 1 at the transition point becomes challenging, contributing to the greater stability of Cycle 1 compared to Cycle 2. In these instances, aside from the directions of the two limit cycles, there exist escape routes toward other attractors. This results in sustained locomotion and an inertial response for transition, as returning to the two limit cycles incurs considerably higher costs.

Since the Gaussian noise is used in our model for the landscape analysis, we hope to have some discussions on the roles of Gaussian noise. Gaussian white noise is commonly employed in biological modeling and stems from diverse sources.<sup>18,27,33</sup> These sources categorize white noise into sensory noise, cellular noise, electrical noise, and synaptic noise.<sup>34</sup> In our model, Gaussian noise plays a crucial role in facilitating escape from attractors. This departure from stable states helps initiate the pirouette behavior. The primary attribution of these roles can be ascribed to electrical and synaptic noise, as behavior persistence appears to be more intrinsic and less susceptible to external stimuli and neural variability. On the other hand, Gaussian noise plays a vital role in the transition domain and the creation of diverse cyclic trajectories, contributing to the overall diversity of pirouettes. This diversity is mainly attributed to sensory noise, given that the choices of strategies are inherently adaptive to external stimuli. In short, sensory noise drives the diversity of navigation strategies, whereas electrical and synaptic noise contributes to the completeness of pirouette behaviors.

### Energy landscape confirms and predicts neural functions and circuits

Having unveiled the intricate transition patterns governing *C. elegans'* locomotion and the corresponding dynamical structure, our focus now shifts to elucidating the pivotal roles of specific neurons for locomotion. This exploration leverages insights from two limit cycles and corresponding energy landscape. Delving into the dynamics of activity within two limit cycles and the landscape's contour, we observe that the Forward state is accompanied by the high levels of AVBR activity, while the Sustain reverse state is always accompanied by the peaks of AVAR activity (Figure 5A). This substantiates the roles of AVBR in fostering forward locomotion and AVAR in supporting backward locomotion. Notably, the landscape configurations for AVAR and AVBR adopt an "L" shape (Figure 5A), suggesting that both neurons might not simultaneously reach the action potential. Additionally, in two limit cycles, RIVR's activity peeks at the start of ventral turns during the initial phase of slow down (Figure 5B), confirming its pivotal role in initiating  $\Omega$  turn. This observation also predicts the potential contribution of RIVR activity to the preparatory phase before reversal, given that the Slow state precludes the transition to reversal. Similarly, analysis of the energy landscape with two limit cycles points to RIM and AVE as promoters of backward locomotion (Figures S5C and S5D), RIB as a facilitator of forward locomotion and turns (Figure S5B), and AVE as a potential initiator of ventral turns (Figure S5C). Furthermore, an analysis of activity within two limit cycles uncovers that AIB follows an ascending trajectory spanning the entire reverse phase and the initial segment of ventral turns (Figures S6A and S5D). This observation underscores the potential of AIB in facilitating turns and signaling reverse behavior. The patterns of the energy landscape for pairs such as RIMR and AVAL, AVBR and RIBL, and AVER and RIMR strikingly resemble straight lines with positive correlations (Figures S5A–S5C), hinting at the possibility that these neuron pairs might belong to the same functional module for navigation.

Sequential activation can be identified through the analysis of the two limit cycles, given that the locomotion patterns predominantly revolve around these cycles. An intriguing pattern emerges from the projection of two cycles: an impulse in AIBL is succeeded by a delayed impulse in RIVL during forward and turning states (Figure S6A). The observed pattern strongly suggests sequential activation between these two neurons. It also confirms the earlier findings that connections between AIB and RIV contribute to the sequential activation, along with the feedforward coupling between the backward and turning module.<sup>3</sup> Moreover, similar sequential activations "AVAL  $\rightarrow$  RIMR" and "AVER  $\rightarrow$  RIMR" can be indicated by the projections of limit cycles (Figures S5A and S5C). Taking into account neural connectivity,<sup>35,36</sup> our observations unveil a segment of a neural circuit involving AVA, RIM, and subsequently AVE/AIB. Notably, this neural circuit aligns with components of the circuit for navigations.<sup>22,31</sup> This discovery underscores our model's capability to identify crucial neural circuits that govern locomotion strategies.

### The simulation of inhibition efficiently unveils the function of specific neurons

To depict the impact of inhibiting certain neurons in our model, we introduce an inhibitory force (see more details in STAR Methods) targeted at certain neurons. This intervention is designed to explore its impact on the locomotion behaviors and corresponding dynamical structure (Figures 6A and 6B). Following inhibition, trajectories originating from Cycle 1 uniformly converge toward new attractors in the Forward and Sustain reverse states (Figures 6C and 6D). Examination of the landscape post-inhibition of RIV reveals the disruption of the original tube-like orbits of the two cycles. The only remaining structure is two branches containing the Forward and Sustain reverse basins, and the region associated with the Ventral turn states is almost submerged by the infeasible areas. These results highlight that inhibiting RIV effectively suppresses ventral turns, providing an explanation for previous observations that the elimination of RIV leads to a reduction in the frequency of  $\Omega$  turns.<sup>3,31</sup> Since two branches correspond to the forward and backward locomotion and an additional barrier separates these two states, inhibition of neuron RIV might also contribute to a decreased frequency of behavioral transitions. Importantly, the changes in the potential landscape during the increment in inhibition levels vividly depict the diminishing process of ventral turns (Figure S7).

To quantify the impact of inhibiting certain neurons, we conduct calculations on the state probability after inhibiting individual neurons (Table 1). This particular analysis of state probability serves as both validation and prediction of the functional roles of distinct

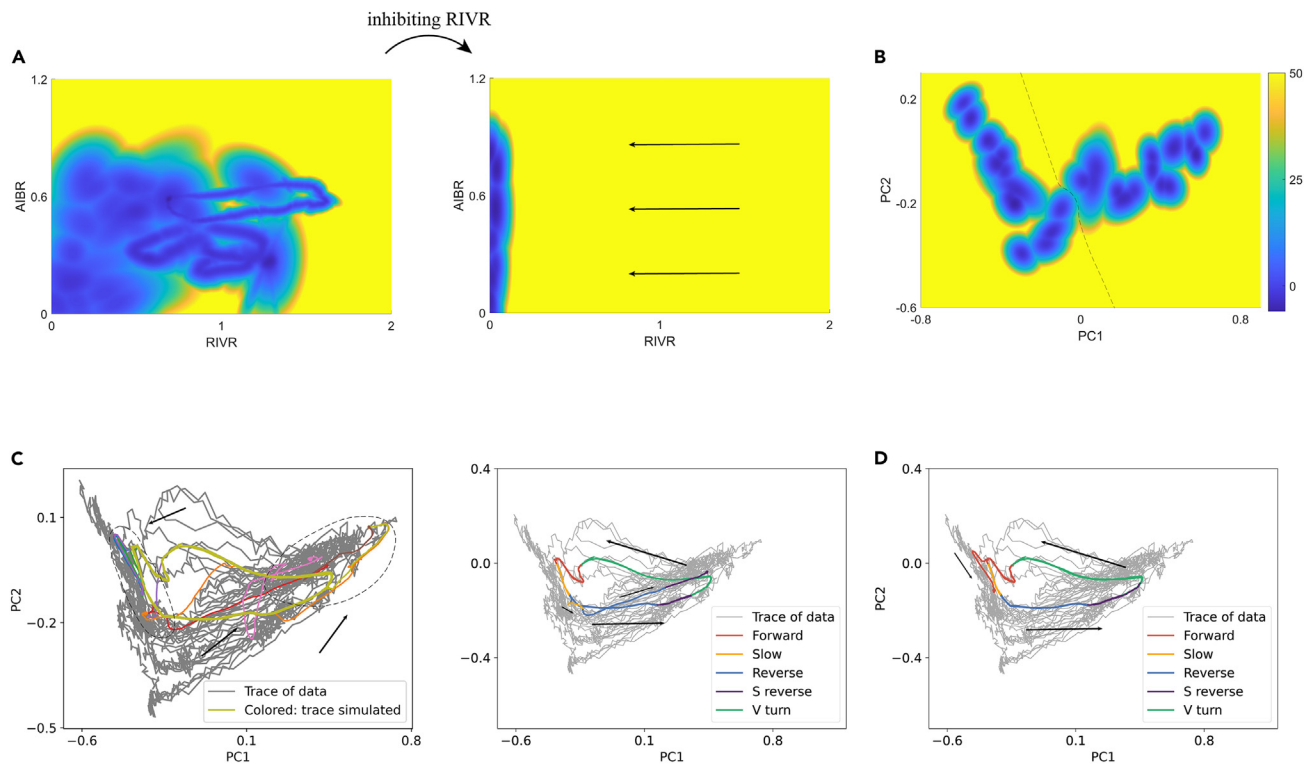


**Figure 6. Disabling RIV inhibits the transition between forward and backward locomotion and reduces the likelihood of ventral turns**

(A) The energy landscape after disabling the RIVR (right) compared to before (left), projected onto the space of AIBR and RIVR activity. The feasible region is shifted toward where RIVR activity is 0.

(B) The landscape after disabling the RIVR, projected onto the first two PCs. The feasible set is divided into two branches. The feasible set is split into two branches. The pathway between the Forward state and the Sustain reverse state is disrupted. The area associated with the Ventral Turn states is almost entirely covered by the infeasible regions (compared with Figure 4A).

(C and D) Simulations of neural activity after disabling RIVR, starting from various points within Cycle 1. The trajectories all converge to either the left side (Forward) or the right side (Sustain reverse), depending on their initial location.

neurons. Our observation aligns with established knowledge: AVB promotes forward locomotion,<sup>1,2</sup> AVA promotes backward locomotions<sup>1,2</sup> and RIV underlies the ventral asymmetry of  $\Omega$  turns.<sup>2,31</sup> The decreased probability of forward locomotion states (Forward and Slow) following RIB inhibition verifies the prior conclusions that RIB promotes the speed of forward locomotion but not backward locomotion.<sup>37</sup> Similarly, the diminished occurrence of the Sustain reverse state and the concurrent increase in the Reverse state after inhibiting RIM confirms RIM's involvement in backward locomotion<sup>3</sup> and supports earlier observations that eliminating RIM neurons results in inappropriate persistence of short reversals after food removal.<sup>31</sup> Besides, our simulation also verifies that inhibiting neuron RIV during turns restored mechanosensory-evoked reversals.<sup>38</sup> Earlier studies have indicated that inhibiting AIB results in a reduction in  $\Omega$  turns (Dorsal/Ventral turn) and long reversals (Sustain reverse), while leads to an increase of short reverse (Reverse state).<sup>31</sup> Our simulation for AIBL repeats this phenomenon and the simulation for AIBR supports the statement for decreases of turns. However, the outcome of inhibiting AIBR manifests in more frequent long reversals and fewer short reversals, suggesting that AIBL and AIBR may play different roles in the decoding of behaviors for navigation. Furthermore, our simulations offer predictive insights, indicating that RID may indeed promote forward locomotion, while neuron ALA, known for inducing the sleep phenotype,<sup>39</sup> might not significantly contribute to the locomotion within the navigation. The observed decrease in dorsal turns after inhibiting RIM underscores RIM's specific importance in dorsal turns.

In the neural system some neurons function as highly connected and pivotal network hubs, facilitating communication between functionally separated local clusters and exhibiting tightly coupled gene expression.<sup>40–42</sup> Thus, identifying these hub neurons, even without explicit neural connectivity information, is crucial for a better understanding of neural network mechanisms. We quantify the impact of inhibiting specific neurons by calculating the KL divergence of state probability (Figure S8). Our analysis reveals a positive correlation between KL divergence and the degree of neurons<sup>35,36</sup> in the neural connectivity (with a correlation coefficient of  $r = 0.6101$ ). It also indicates that neurons ALA, RID and RIV may be the periphery part while AIB, AVA, AVE and RIM are more like hubs. Notably, recent studies have also identified AIB, AVA, and AVE as hubs.<sup>40,41</sup> Thus, our model may serve as an indicator for identifying neurons that function as hubs in the absence of explicit connectivity information.

**Table 1. The probability of states after different neurons being inhibited**

Neurons	Forward	Slow	Dorsal turn	Ventral turn	Reverse	Sustain reverse	Supporting references& Predictions
DEFAULT	17.00%	16.87%	9.59%	9.58%	10.15%	36.81%	The default state probability.
AIBL	<b>4.03%</b>	7.23%	<b>0.19%</b>	<b>0.29%</b>	50.09%	38.18%	Turns, Sustain reverse <sup>3,31</sup>
AIBR	<b>1.47%</b>	7.68%	<b>0.04%</b>	<b>0.33%</b>	8.28%	82.19%	
ALA	17.47%	20.53%	4.40%	21.31%	8.15%	28.13%	Unrelated to the locomotion
AVAL	26.80%	16.39%	5.00%	20.44%	28.67%	<b>2.69%</b>	Sustain reverse <sup>1,2,20</sup>
AVAR	26.09%	7.37%	<b>1.55%</b>	32.17%	22.31%	<b>10.52%</b>	
AVBL	33.56%	<b>2.39%</b>	6.41%	9.83%	11.15%	36.65%	Forward locomotion
AVBR	<b>2.94%</b>	<b>2.60%</b>	15.30%	15.40%	20.71%	43.06%	(Forward and Slow) <sup>1,2,20</sup>
AVER	17.20%	<b>3.47%</b>	<b>1.70%</b>	<b>0.29%</b>	8.42%	68.93%	Reverse, Sustain reverse <sup>1,2</sup>
RIBL	<b>5.04%</b>	<b>2.19%</b>	15.53%	11.26%	13.89%	52.09%	Forward (promote only forward locomotion speed) <sup>37</sup>
RID	<b>6.27%</b>	15.54%	7.69%	12.52%	8.37%	49.61%	Promote Forward locomotion
RIML	8.97%	<b>5.19%</b>	<b>0.51%</b>	<b>0.21%</b>	74.43%*	<b>10.70%</b>	Promote Sustain reverse <sup>3</sup> and
RIMR	<b>3.56%</b>	7.97%	<b>2.99%</b>	7.07%	63.60%*	14.80%	high probability of short reversals (Reverse state) after inhibition <sup>31</sup>
RIVL	<b>4.71%</b>	12.49%	21.45%	<b>0.51%</b>	9.36%	51.49%	Ventral turn <sup>3,31</sup>
RIVR	9.43%	8.12%	6.17%	<b>2.10%</b>	6.98%	67.20%	

States with a probability decrease of less than 40% after inhibition are formulated in bold, while those with a probability increase of more than six times are labeled with symbol \*.

## DISCUSSION

In this study, we utilize a deep-learning approach to reconstruct the neural dynamics of *C. elegans*. We introduce two methods: the clustering division method and a deep neural network (DNN) strategy, to explain the locomotion behaviors observed in our simulations. Our DNN model stands out from other artificial neural network models for *C. elegans* by not only reconstructing the neural dynamics but also enabling an in-depth exploration of the dynamical mechanisms that govern *C. elegans*' locomotion. The dynamical analysis yields several advantages. Firstly, it helps us to capture the key dynamical structure, such as two limit cycles and attractors in the transition area, offering insights into the flexible patterns of locomotion. Second, the dynamical system allows for the introduction of noise, providing a platform to study the roles of noise. It indicates that appropriate noise contributes to the complexity and diversity of pirouette strategies. Thirdly, the reconstructed dynamics lays the foundation for the calculation of the energy landscape, which offers effective tools for investigating the global dynamical properties and explains the mechanisms of strategies switching. Finally, the reconstructed dynamics enables the simulation for inhibiting specific neurons, aiding in the revelation of the distinct roles played by each neuron.

Our DNN model helps investigate the dynamical properties by reconstructing neural dynamics from data. However, there also exist other approaches for investigating the dynamical properties of data. Recent studies have employed delay-embedding methods to linearize the dynamics of data in a higher-dimensional space.<sup>43</sup> This linearized approach provides potent methods for comparing the similarity between two datasets by introducing a distance function based on linearized dynamics. Compared to these approaches, our reconstructed dynamics preserves the original activity space, enabling us to investigate more biophysical properties by introducing the energy landscape and simulating the inhibition of specific neurons.

Electrical synapses play diverse roles in neuronal development, circuit regulation, and stress conditions.<sup>44,45</sup> In our dynamical model, the energy landscape offers an intuitive method to explore the impact of gap junctions. The energy landscape projected onto pairs like AIBL and RIVR, and AIBL and RIVL, reveals that the former pair can be almost regarded as the latter one compressed into a diagonal line (Figures S6A and S6B). Essentially, the dynamics between the former pair is approximated by introducing a "compressing force" into the dynamics of the latter pairs (see more details in STAR Methods). In the neural network, the connectivity of these two pairs differs due to an additional electrical connection in the former pair.<sup>35,36</sup> Therefore, the "compressing force" may serve to approximate and intuitively depict the influence of electrical junctions.

The dynamical results from our DNN model reveal a fundamental navigation strategy in *C. elegans*, involving switching between two limit cycles. During our study, *C. elegans* was immobilized in a microfluidic chamber, and the recording began within 5 min after removal from food.<sup>20</sup> The navigation may encompass both local search foraging behavior and escape and avoidance behaviors when contacting the walls.<sup>46,47</sup> The dynamical structure, characterized by two limit cycles, offers an explanation for the navigation strategy in both scenarios. In local search, the selection of Cycle 2 at transition points might assist the worm in deciding whether to engage in precise local foraging. In escape or avoidance behaviors, the choice of Cycle 2 at transition points may determine whether the current direction is suitable or if the worm should explore another direction for escape or avoidance. In short, the dynamical structure enhances our understanding of *C. elegans* navigation in various circumstances.

### Limitations of the study

While our study introduces methods to reconstruct the neural dynamics of *C. elegans* and investigate the underlying mechanisms for locomotion, there are several limitations associated with our approaches. First, different neurons in many systems exhibit distinct time constants, resulting in varied dynamics timescales. However, our DNN model currently has limitations in effectively evaluating these time constants. Future research combining the neural activity data with the detailed neural connectivity information holds the potential to reveal various time constants governing neural dynamics in a more comprehensive manner. Another limitation in our model is the assumption of noise form. While we assume the noise following a Gaussian white noise pattern, it is acknowledged that noise in biological systems might not strictly conform to a Gaussian distribution. This assumption is rooted in the context of our approaches, which involve introducing the energy landscape of *C. elegans*' neural system. Our methods for quantifying the energy landscape rely on the assumption that the noise adheres to a Gaussian distribution. In instances where the noise is not Gaussian, previous methods often need the numerical integral, which is very challenging in high-dimensional space. Consequently, we limit our current study to these simplified cases, with the anticipation of addressing non-Gaussian scenarios in future investigations.

### STAR★METHODS

Detailed methods are provided in the online version of this paper and include the following:

- KEY RESOURCES TABLE
- RESOURCE AVAILABILITY
  - Lead contact
  - Materials availability
  - Data and code availability
- METHOD DETAILS
  - Choice of the phase space
  - The deep learning method for reconstructing neural dynamics
  - Calculation of state transition probability and behavioral decoding of phase space
  - The energy landscape of *C. elegans*' neural dynamics
  - The landscape construction for limit cycle system
- QUANTIFICATION AND STATISTICAL ANALYSIS

### SUPPLEMENTAL INFORMATION

Supplemental information can be found online at <https://doi.org/10.1016/j.isci.2024.109759>.

### ACKNOWLEDGMENTS

C.L. is supported by the National Key R&D Program of China (2019YFA0709502) and the National Natural Science Foundation of China (12171102). Y.Y. thanks for the support from the Science and Technology Innovation 2030 - Brain Science and Brain-Inspired Intelligence Project (2021ZD0201301), the Shanghai Municipal Science and Technology Major Project (2018SHZDZX01) and ZJLab, Shanghai Municipal Science and Technology Committee of Shanghai outstanding academic leaders plan (21XD1400400).

### AUTHOR CONTRIBUTIONS

C.L. and R.Z. designed the research; R.Z. performed the research; R.Z., Y.Y., and C.L. analyzed the data; R.Z. and C.L. wrote the paper; R.Z., Y.Y., and C.L. revised the paper.

### DECLARATION OF INTERESTS

The authors declare no conflict of interest.

Received: October 7, 2023

Revised: January 27, 2024

Accepted: April 15, 2024

Published: April 17, 2024

### REFERENCES

1. Lanza, E., Di Angelantonio, S., Gosti, G., Ruocco, G., and Folli, V. (2021). A recurrent neural network model of *C. elegans* responses to aversive stimuli. *Neurocomputing* 430, 1–13.
2. Soh, Z., Sakamoto, K., Suzuki, M., Iino, Y., and Tsuji, T. (2018). A computational model of internal representations of chemical gradients in environments for chemotaxis of *Caenorhabditis elegans*. *Sci. Rep.* 8, 17190–17214.
3. Wang, Y., Zhang, X., Xin, Q., Hung, W., Florman, J., Huo, J., Xu, T., Xie, Y., Alkema, M.J., Zhen, M., and Wen, Q. (2020). Flexible motor sequence generation during stereotyped escape responses. *Elife* 9, e56942.

4. Shen, Q., and Liu, Z. (2021). Remote firing propagation in the neural network of *C. elegans*. *Phys. Rev. E* **103**, 052414.
5. Brennan, C., and Proekt, A. (2019). A quantitative model of conserved macroscopic dynamics predicts future motor commands. *Elife* **8**, e46814.
6. Morrison, M., Fieseler, C., and Kutz, J.N. (2020). Nonlinear control in the nematode *C. elegans*. *Front. Comput. Neurosci.* **14**, 616639.
7. Pereda, A.E. (2019). Neuroscience: the hidden diversity of electrical synapses. *Curr. Biol.* **29**, 2105–2106.
8. Varshney, L.R., Chen, B.L., Paniagua, E., Hall, D.H., and Chklovskii, D.B. (2011). Structural properties of the *Caenorhabditis elegans* neuronal network. *PLoS Comput. Biol.* **7**, e1001066.
9. Liu, F., Meamardoost, S., Gunawan, R., Komiyama, T., Mewes, C., Zhang, Y., Hwang, E., and Wang, L. (2022). Deep learning for neural decoding in motor cortex. *J. Neural. Eng.* **19**, 056021.
10. Livezey, J.A., and Glaser, J.I. (2021). Deep learning approaches for neural decoding across architectures and recording modalities. *Brief. Bioinform.* **22**, 1577–1591.
11. Glaser, J.I., Benjamin, A.S., Chowdhury, R.H., Perich, M.G., Miller, L.E., and Kording, K.P. (2020). Machine learning for neural decoding. *Eneuro* **7**, ENEURO.0506-19.2020.
12. Trevino, A.E., Müller, F., Andersen, J., Sundaram, L., Kathiria, A., Scherbina, A., Farh, K., Chang, H.Y., Paşca, A.M., Kundaje, A., et al. (2021). Chromatin and gene-regulatory dynamics of the developing human cerebral cortex at single-cell resolution. *Cell* **184**, 5053–5069.e23.
13. Glaser, J.I., Benjamin, A.S., Farhoodi, R., and Kording, K.P. (2019). The roles of supervised machine learning in systems neuroscience. *Prog. Neurobiol.* **175**, 126–137.
14. Kalinin, A.A., Higgins, G.A., Reamaron, N., Sorousmehr, S., Allyn-Feuer, A., Dinov, I.D., Najarian, K., and Athey, B.D. (2018). Deep learning in pharmacogenomics: from gene regulation to patient stratification. *Pharmacogenomics* **19**, 629–650.
15. Wang, Z., Wang, D., Li, C., Xu, Y., Li, H., and Bao, Z. (2018). Deep reinforcement learning of cell movement in the early stage of *C. elegans* embryogenesis. *Bioinformatics* **34**, 3169–3177.
16. Iino, Y., and Yoshida, K. (2009). Parallel use of two behavioral mechanisms for chemotaxis in *Caenorhabditis elegans*. *J. Neurosci.* **29**, 5370–5380.
17. Chen, F., and Li, C. (2022). Inferring structural and dynamical properties of gene networks from data with deep learning. *NAR Genom. Bioinform.* **4**, lqac068.
18. Ye, L., and Li, C. (2021). Quantifying the landscape of decision making from spiking neural networks. *Front. Comput. Neurosci.* **15**, 740601.
19. Yan, H., Zhao, L., Hu, L., Wang, X., Wang, E., and Wang, J. (2013). Nonequilibrium landscape theory of neural networks. *Proc. Natl. Acad. Sci. USA* **110**, E4185–E4194.
20. Kato, S., Kaplan, H.S., Schrödel, T., Skora, S., Lindsay, T.H., Yemini, E., Lockery, S., and Zimmer, M. (2015). Global brain dynamics embed the motor command sequence of *Caenorhabditis elegans*. *Cell* **163**, 656–669.
21. Calhoun, A.J., Chalasani, S.H., and Sharpee, T.O. (2014). Maximally informative foraging by *Caenorhabditis elegans*. *Elife* **3**, e04220.
22. López-Cruz, A., Sordillo, A., Pokala, N., Liu, Q., McGrath, P.T., and Bargmann, C.I. (2019). Parallel multimodal circuits control an innate foraging behavior. *Neuron* **102**, 407–419.e8.
23. Bendena, W.G., Boudreau, J.R., Papanicolaou, T., Maltby, M., Tobe, S.S., and Chin-Sang, I.D. (2008). A *Caenorhabditis elegans* allatostatin/galanin-like receptor NPR-9 inhibits local search behavior in response to feeding cues. *Proc. Natl. Acad. Sci. USA* **105**, 1339–1342.
24. Yu, Y., Zhi, L., Wu, Q., Jing, L., and Wang, D. (2018). NPR-9 regulates the innate immune response in *Caenorhabditis elegans* by antagonizing the activity of AIB interneurons. *Cell. Mol. Immunol.* **15**, 27–37.
25. Ji, P., Wang, Y., Peron, T., Li, C., Nagler, J., and Du, J. (2023). Structure and function in artificial, zebrafish and human neural networks. *Phys. Life Rev.* **45**, 74–111.
26. Ye, L., Feng, J., and Li, C. (2023). Controlling brain dynamics: Landscape and transition path for working memory. *PLoS Comput. Biol.* **19**, e1011446.
27. Li, C., and Wang, J. (2014). Landscape and flux reveal a new global view and physical quantification of mammalian cell cycle. *Proc. Natl. Acad. Sci. USA* **111**, 14130–14135.
28. Li, C., and Wang, J. (2013). Quantifying cell fate decisions for differentiation and reprogramming of a human stem cell network: landscape and biological paths. *PLoS Comput. Biol.* **9**, e1003165.
29. Pillai, M., Chen, Z., Jolly, M.K., and Li, C. (2022). Quantitative landscapes reveal trajectories of cell-state transitions associated with drug resistance in melanoma. *iScience* **25**, 105499.
30. Wang, J., Xu, L., and Wang, E. (2008). Potential landscape and flux framework of nonequilibrium networks: Robustness, dissipation, and coherence of biochemical oscillations. *Proc. Natl. Acad. Sci. USA* **105**, 12271–12276.
31. Gray, J.M., Hill, J.J., and Bargmann, C.I. (2005). A circuit for navigation in *Caenorhabditis elegans*. *Proc. Natl. Acad. Sci. USA* **102**, 3184–3191.
32. Van Kampen, N.G. (1992). *Stochastic Processes in Chemistry and Physics*, 1st Ed (North-Holland), pp. 120–127.
33. Hasani, R., Ferrari, G., Yamamoto, H., Tani, T., and Prati, E. (2021). Role of Noise in Spontaneous Activity of Networks of Neurons on Patterned Silicon Emulated by Noise-activated CMOS Neural Nanoelectronic Circuits. *Nano Ex.* **2**, 020025.
34. Faisal, A.A., Selen, L.P.J., and Wolpert, D.M. (2008). Noise in the nervous system. *Nat. Rev. Neurosci.* **9**, 292–303.
35. Chen, B. (2007). *Neuronal network of C. elegans: from anatomy to behavior*. PhD thesis (The Watson School of Biological Sciences).
36. Cook, S.J., Jarrell, T.A., Brittin, C.A., Wang, Y., Bloniarz, A.E., Yakovlev, M.A., Nguyen, K.C.Q., Tang, L.T.H., Bayer, E.A., Duerr, J.S., et al. (2019). Whole-animal connectomes of both *Caenorhabditis elegans* sexes. *Nature* **571**, 63–71.
37. Li, Z., Liu, J., Zheng, M., and Xu, X.Z.S. (2014). Encoding of both analog-and digital-like behavioral outputs by one *C. elegans* interneuron. *Cell* **159**, 751–765.
38. Kumar, S., Sharma, A.K., Tran, A., Liu, M., and Leifer, A.M. (2023). Inhibitory feedback from the motor circuit gates mechanosensory processing in *caenorhabditis elegans*. *PLoS Biol.* **21**, e3002280.
39. Nath, R.D., Chow, E.S., Wang, H., Schwarz, E.M., and Sternberg, P.W. (2016). *C. elegans* stress-induced sleep emerges from the collective action of multiple neuropeptides. *Curr. Biol.* **26**, 2446–2455.
40. Ripoll-Sánchez, L., Watteyne, J., Sun, H., Fernandez, R., Taylor, S.R., Weinreb, A., Bentley, B.L., Hammarlund, M., Miller, D.M., 3rd, Hobert, O., et al. (2023). The neuropeptidergic connectome of *c. elegans*. *Neuron* **111**, 3570–3589.e5.
41. Arnatkevičiūtė, A., Fulcher, B.D., Pocock, R., and Fornito, A. (2018). Hub connectivity, neuronal diversity, and gene expression in the *caenorhabditis elegans* connectome. *PLoS Comput. Biol.* **14**, 1–32.
42. Uzel, K., Kato, S., and Zimmer, M. (2022). A set of hub neurons and non-local connectivity features support global brain dynamics in *c. elegans*. *Curr. Biol.* **32**, 3443–3459.e8.
43. Ostrow, M., Eisen, A., Kozachkov, L., and Fiete, I. (2023). Beyond geometry: Comparing the temporal structure of computation in neural circuits with dynamical similarity analysis. Preprint at arXiv. <https://doi.org/10.48550/arXiv.2306.10168>.
44. Meng, L., and Yan, D. (2020). NLR-1/CASPR anchors F-actin to promote gap junction formation. *Dev. Cell* **55**, 574–587.e3.
45. Jin, E.J., Park, S., Lyu, X., and Jin, Y. (2020). Gap junctions: historical discoveries and new findings in the *Caenorhabditis elegans* nervous system. *Biol. Open* **9**, bio053983.
46. Pirri, J.K., and Alkema, M.J. (2012). The neuroethology of *c. elegans* escape. *Curr. Opin. Neurobiol.* **22**, 187–193.
47. Schild, L.C., and Glauser, D.A. (2013). Dynamic switching between escape and avoidance regimes reduces *caenorhabditis elegans* exposure to noxious heat. *Nat. Commun.* **4**, 2198.
48. Hu G (1994) *Stochastic forces and nonlinear systems*. Shanghai Scientific and Technological Education, Shanghai, China: 68–74.

## STAR★METHODS

### KEY RESOURCES TABLE

REAGENT or RESOURCE	SOURCE	IDENTIFIER
Deposited data		
Kato2015 whole brain imaging data	Kato et al. <sup>20</sup>	<a href="https://osf.io/2395t/">https://osf.io/2395t/</a>
Software and algorithms		
MATLAB R2020b	Commercially Available Software (Mathworks)	N/A
Pytorch 1.13.0	GitHub	<a href="https://pytorch.org/">https://pytorch.org/</a>
Python 3.8	Python Software Foundation	<a href="https://www.python.org/">https://www.python.org/</a>
Custom computer code	This paper	<a href="https://github.com/minecraburn/DNN_for_Celegans">https://github.com/minecraburn/DNN_for_Celegans</a>

### RESOURCE AVAILABILITY

#### Lead contact

Further information and requests can be directed to the lead contact, Chunhe Li ([chunheli@fudan.edu.cn](mailto:chunheli@fudan.edu.cn)).

#### Materials availability

This study did not generate new physical materials.

#### Data and code availability

- All data used in this study is publicly available: Kato2015 whole brain imaging data is available at <https://osf.io/2395t/>.
- All original code has been deposited at [https://github.com/minecraburn/DNN\\_for\\_Celegans](https://github.com/minecraburn/DNN_for_Celegans) and is publicly available as of the date of publication.
- Any additional information required to reanalyze the data reported in this article is available from the [lead contact](#) on request.

### METHOD DETAILS

#### Choice of the phase space

The neural activity of about 100 neurons in the head ganglia was recorded simultaneously for five *elegans* through  $Ca^{2+}$  Imaging by Kato et al.,<sup>20</sup> with fixed frame rates (2.90, 2.90, 2.83, 3.07, 2.80 frames per second for five animals respectively). Our model is based on this dataset. Each *elegans* was immobilized in a microfluidic chamber. Recordings were started within 5 min after removal from food with constant 21%  $O_2$ , and the recordings last for 18 min. Only part of the 100+ neurons can be recognized and labeled names. There are only 21 commonly recognized neurons for five animals, and we choose  $d = 14$  common neurons to span our phase space. The 14 neurons are AIB(L/R), ALA, AVA(L/R), AVB(L/R), AVER, RIBL, RID, RIM(L/R), RIV(L/R). The trace data of activity for five animals can be noted as  $\{x_t^i\} (i = 1, \dots, n. 1 \leq t \leq T_i)$  for  $n = 5$ . Each  $x_t^i$  means a 14-dimension ( $d = 14$ ) vector in the phase space. We also apply the normalization and principal components analysis of the trace data  $\{x_t^i\}$  to get the principal components for illustrating the trajectories and landscapes.

#### The deep learning method for reconstructing neural dynamics

In this section, we will introduce a deep-learning method to approach the dynamic force. Since we apply our method to five animals separately, in this section we will take the 1st animal for example. Following previous works,<sup>19</sup> the change in neural activity of *C. elegans* can be described as a stochastic dynamical system formulated by (Equation 1) where  $\epsilon = (\epsilon_1(t), \dots, \epsilon_d(t))^T$  is the  $d$ -dimensional independent Gaussian white noise which means

$$\mathbb{E}[\epsilon_i(t)] = 0, \quad (\text{Equation 4})$$

$$\mathbb{E}[\epsilon_i(t)\epsilon_j(\hat{t})] = 2D\delta_{ij}\delta_0(t - \hat{t}).$$

Here,  $\delta_0$  is the Dirac delta function. For simplicity, we assume the white noise here is homogeneous and independent of the current neural activity, so  $D$  is the constant diffusion coefficient and

$$\delta_{ij} = \begin{cases} 1, & i = j \\ 0, & i \neq j \end{cases} \quad (\text{Equation 5})$$

We use the deep learning method and employ a curve fitting method to learn the dynamic force from the data. The key point is to use a function  $\hat{F}$  to approximate the dynamics  $F$  in the stochastic dynamical system (1). In the dynamics reconstruction process, the stochastic term is omitted. In other words, the data trajectories  $\{x_t^i\}$  can be generated by Equation 1. Note  $\delta t$  as the time between two frames of the data trajectories  $\{x_t^i\}$  (between  $x_t^i$  and  $x_{t+\delta t}^i$ ). By dividing  $\delta t$  into  $s$  segments, the dynamical process can be discretized using the single-step explicit scheme and we can define the evolution map as

$$g_{\hat{F}} : x \rightarrow x + \frac{\delta t}{s} \hat{F}(x).$$

For a nice approximation  $\hat{F}$  of  $F$ , the position (i.e.,  $g_{\hat{F}}^{ms}(x_t^i)$ ) after time  $m\delta t$  in the dynamical system for  $\hat{F}$  should be close to that (i.e.,  $g_F^{ms}$ ) in the dynamical system for  $F$  (here  $m, s$  are hyperparameters). Since in our model we assume that the data trajectories can be generated by the dynamical system with  $F$ , we immediately have  $g_F^{ms}(x_t^i) = x_{t+m}^i$ . Therefore, the error of the approximation can be quantified by the distance between  $x_{t+m}^i$  and  $g_{\hat{F}}^{ms}(x_t^i)$ . To reduce the influence of the Gaussian noise, we also introduce a smoothed data trace for approximation

$$\bar{x}_t = \frac{c_1 x_{t-1}^i + x_t^i + c_1 x_{t+1}^i}{2c_1 + 1}, \quad (\text{Equation 6})$$

where  $c_1$  is the smooth coefficient. Since for a test problem  $F(x) = ax (a > 0)$ ,  $g_F^m(x)$  will increase exponentially, an infeasible initialization for the coefficient will cause numerical issues in computing the loss function and may result in global non-convergence in optimization for the coefficients for neural networks. Therefore, instead of using the neural network to learn  $F$  directly, we use the network to approximate

$$f(x) = \hat{F}(x) + kx, \quad (\text{Equation 7})$$

where  $k > 0$  is the correction coefficient. At the initial stage, the approximate dynamic force  $\hat{F}(x) = f(x) - kx$  will be dominated by the term  $-kx$ , which overcomes the numerical problem mentioned above.

Now we can define the error of approximation, i.e., the loss function for the neural network. For  $t \leq T_i - m - 1$ , the single error  $\zeta$  at  $x_t^i$  with a duration of  $m\delta t$  is,

$$\zeta_{\hat{F}}(x_t^i) = \sum_{k=1}^m \left\| \bar{x}_{t+k} - g_{\hat{F}}^{ks}(x_t^i) \right\|_2 = \sum_{k=1}^m \left\| \bar{x}_{t+k} - g_{\hat{F}-kx}^{ks}(x_t^i) \right\|_2. \quad (\text{Equation 8})$$

The total loss function  $\varepsilon(\hat{F})$  will be the average of all single error

$$\varepsilon(\hat{F}) = \sum_{t=1}^{T_1-m} \zeta_{\hat{F}}(x_t^1). \quad (\text{Equation 9})$$

We use a DNN to construct  $\hat{F}$ . The neural network model we use contains three hidden layers. All the hidden layers contain 120 nodes. The number of neurons in the input layers and output layers is equal to the number of neurons in our model, i.e., the  $d = 14$  consistently and unequivocally identified neurons. The neural network is trained by the standard gradient optimization (RMSprop optimizer in Pytorch). The learning rate starts from  $10^{-2}$ , and decreases when the loss function does not decrease for several epochs, until less than  $10^{-8}$ . Finally, the trained DNN can be represented as a function with the neural dynamics input  $x$  and output as part of the dynamics

$$\tilde{f}(x) = b_4 + w_4 \cdot \text{Sigmoid}\{b_3 + w_3 \cdot \text{ReLU}[b_2 + w_2 \cdot \text{ReLU}(b_1 + w_1 \cdot x)]\}.$$

In practice, we find that too large segment coefficient  $m, s$  in (Equations 8 and 9) will cause the divergence, and too small  $m, s$  will cause the unfitness for longer traces. In practice,  $s = 3$  and  $m = 2$  is a practical setting. Besides we find the correction coefficients  $k = 1$  in (Equation 7) and smooth coefficient  $c_1 = 1$  in (Equation 6) are suitable.

After the neural network is trained and the dynamic force  $F(x) = f(x) - kx$  is obtained, we use the discretization of the dynamical system (1) to simulate the trace. Fixing a start  $x_0$ , we can generate an independent sequence  $\{r_i\} \sim N(0, \sigma^2 I)$  and get the simulate trace by

$$x(i\Delta t) = x((i-1)\Delta t) + F(x((i-1)\Delta t))\Delta t + r_i \sqrt{\Delta t}.$$

Since the data points are confined in a low-dimensional space, the areas around the data points are most meaningful. Therefore, we pick the start point  $x_0$  randomly around the data point:

$$t \sim \text{Uniform}(1, T_i),$$

$$\tau \sim N(0, \hat{\sigma}^2),$$

$$x_0 \leftarrow x_t^i + \tau,$$

where  $\hat{\sigma}^2$  is the MLE of covariance in (Equation 14). To identify the attractors in the stationary points, we conduct additional simulations starting from points neighboring these stationary points. We record the rates at which the trajectories returned to these points and those with returning rates exceeding 95% will be identified as attractors.

We also investigate the effects of inhibiting specific neurons in our model. When targeting the inhibition of neuron  $i$ , our objective is to nullify the  $i$ -th neural activity. To achieve this, we introduce an “inhibition force”, and Equation 1 is modified to the following form:

$$\frac{dx}{dt} = (F(x) - c_2(e_i^T \cdot x)e_i) + \epsilon. \quad (\text{Equation 10})$$

Here, the dynamic force  $F$  is now replaced by  $F(x) - c_2(e_i^T \cdot x)e_i$ , where  $e_i$  is a  $d$ -dimension vector with 1 as the  $i$ -th element and 0 as other elements. This introduces an external force to the neural network, and for any neuron activity  $x$ , the output of the DNN serves as the function  $f(x)$ . The modified dynamics are then calculated as  $F(x) - c_2(e_i^T \cdot x)e_i = f(x) - kx - c_2(e_i^T \cdot x)e_i$ . A simple mathematical analysis reveals that selecting a sufficiently large coefficient  $c_2$  will drive the  $i$ -th activity to zero. Therefore, an adequately chosen  $c_2$  serves to inhibit the corresponding neural activity in our model.

Similarly, the “compressing force” between neuron  $i$  and neuron  $j$  can be applied by replacing  $F(x)$  by  $F(x) - c_3(e_i - e_j)(e_i - e_j)^T x$ . The effect of electrical synapses can be modeled by the “compressing force” in our model.

### Calculation of state transition probability and behavioral decoding of phase space

We record all the periods of Slow states with durations less than 0.5 s. Surprisingly, all these Slow states start from two types of turns (Dorsal turn and Ventral turn) and ultimately transition to the Reverse state. Therefore, to distinguish these Slow states, we will refer to them as “Slow2” states, while the others will be denoted as “Slow1” states. The durations of Slow2 states are less than 0.5s and keep for only 1 ~ 2 frames. Now, the  $q = 7$  different states of locomotion of *C. elegans* will be Forward, Slow1, Slow2, Dorsal turn, Ventral turn, Reverse and Sustain reverse, which are represented as the first through seventh states.

To calculate the number of state transitions from state  $i$  to state  $j$ , we can use the statistic:

$$N_{i \rightarrow j} = \sum_{k=1}^n \#\{t : \text{State}(x_t^k) = i \text{ and } \text{State}(x_{t+1}^k) = j\}.$$

The state transition probability can be then calculated by,

$$p_{i \rightarrow j} = \frac{N_{i \rightarrow j}}{\sum_{1 \leq k \leq q, k \neq i} N_{i \rightarrow k}}, p_{i \rightarrow j}^{\text{whole}} = \frac{N_{i \rightarrow j}}{\sum_{1 \leq k, l \leq q, k \neq l} N_{k \rightarrow l}}.$$

To explain the locomotion behaviors in the simulation, we need to extend the behaviors observed in data trajectories across the entire activity space. We introduce two methods for segmenting the activity space into various labeled behaviors: the clustering division method and the DNN method. In the clustering division method, we first apply the clustering on data points with each behavior separately. Using the Agglomerative Hierarchical Clustering on data with norm  $L_2$  and the stopping max radius 0.07, each type of behavior point is divided into clusters with cluster center  $\{y_k^i\} (1 \leq i, 1 \leq k \leq n_i)$ . Finally, behavior  $\iota(x)$  is assigned to the point  $x$  by,

$$\iota(x) = \arg \min_{1 \leq i \leq q} \left\{ \min_{1 \leq k \leq n_i} \|x - y_k^i\|_2 \right\}. \quad (\text{Equation 11})$$

In the DNN method, we similarly use the neural network to give the behavior series. A net with three hidden layers of all 120 nodes and the activation functions ReLU, ReLU, Sigmoid sequentially is employed. Obviously, the input size is  $d = 14$ , the size of phase space, and the output size is  $q = 7$ , the number of states. The neural activities are taken as input while state predictions are produced as output. We use the behavior series in the imaging dataset to optimize our neural network and use it to give out the behavior series of our simulations.

### The energy landscape of *C. elegans*' neural dynamics

To globally explore the dynamical structure, we introduce the energy landscape approach. Firstly, the neural systems can be described by the stochastic system (Equation 1). The steady probability distribution can be formulated by the Fokker-Planck equation:

$$P_{ss}(x) \nabla F(x) + F(x) \cdot \nabla P_{ss}(x) = \Delta P_{ss}(x) \quad (\text{Equation 12})$$

with boundary condition,

$$(F(x)P_{ss}(x, t) - D \nabla P_{ss}(x, t)) \cdot \overrightarrow{n(x)} = 0 \quad x \in \Gamma, \quad (\text{Equation 13})$$

where  $D = \frac{\sigma^2}{2}$  is the diffusion coefficient,  $\Gamma = \partial\Omega$  is the boundary for the activity space  $\Omega$  and can be given by  $\{0 \leq x_i \leq 2\}$ . After obtaining the steady probability distribution  $P_{ss}(X)$ , we can then get the energy landscape  $U(z) = -\ln P_{ss}(z)$  and the flux  $J(X)$  from (Equation 2). However,

since the curse of dimensionality rises from the high dimension, it's difficult to solve it directly, and methods approximating the solution are needed.

We first estimate the diffusion coefficient  $D$ , i.e., the half of  $\sigma^2$  using the MLE:

$$\hat{\sigma}^2 = \frac{1}{\delta t \sum_{i=1}^n (T_i - 1)} \sum_{i=1}^n \sum_{t=1}^{T_i-1} \frac{1}{d} \left\| x_{t+1}^i - x_t^i - F(x) \delta t \right\|_2^2. \quad (\text{Equation 14})$$

When the system is a multistable system with only attractors, previous works<sup>17,27,28,32,48</sup> have shown that  $P_{ss}$  can be formulated as a combination of Gaussian distributions:

$$P_{ss}(z) = \frac{1}{(2\pi \det \Sigma(x))^{d/2}} e^{-\frac{1}{2}(z-x)^T \Sigma(x)^{-1} (z-x)}, \quad (\text{Equation 15})$$

and the mean and covariance of each Gaussian distribution can be calculated by the convergent values from the ODEs,

$$\frac{dx}{dt} = F(x(t)), \quad (\text{Equation 16})$$

$$\frac{d\Sigma(t)}{dt} = \Sigma(t)A^T(x(t)) + A(x(t))\Sigma(t) + \sigma^2 I,$$

where the matrix  $A$  is the Jacobi of  $F$ , i.e.,  $A_{ij} = \frac{\partial F_i(x(t))}{\partial x_j(t)}$ . When it comes to the periodic oscillation systems with limit cycles, we need to introduce a new method for calculating landscape. In this approach for periodic oscillation systems, the steady probability can be formulated as,

$$P_{ss}(x) = \frac{\int_C q(z) \frac{1}{(2\pi)^{d/2}} e^{-\frac{1}{2}(x-z)^T \Sigma(z)^{-1} (x-z)} dz}{\int_C q(z) \sqrt{\det \Sigma(z)} dz}, \quad (\text{Equation 17})$$

where  $C = \{x(t) : t \in [0, T_0]\}$  is the limit cycle. For any point  $z$  in  $C$ , let  $v_1(z) = \frac{x'(t)}{\|x'(t)\|_2} = \frac{F(x(t))}{\|F(x(t))\|_2}$  be the direction of limit cycle and  $v_1(z), v_2(z), \dots, v_n(z)$  be an orthonormal basis. Let  $Q = (v_2, \dots, v_n)$ . The covariance matrix  $\Sigma(z)$  rises from the matrix equation,

$$\widehat{\Sigma} Q^T A^T Q + Q^T A Q \widehat{\Sigma} + 2D I_{n-1} = 0 \quad (\text{Equation 18})$$

with  $\Sigma = Q \widehat{\Sigma} Q^T + d_0 v_1 v_1^T$ , where  $d_0$  is a small coefficient. The former one is equivalent to the linear equation,

$$[I \otimes (Q^T A Q) + (Q^T A Q) \otimes I] \text{vec}(\widehat{\Sigma}) = -2D \text{vec}(I_{n-1}). \quad (\text{Equation 19})$$

The density function  $q(t) = q(x(t))$  can be calculated by the following equations,

$$q(t) = e^{\frac{1}{D} \int_0^t g(s)^2 ds} \left[ q(0) - C_0 \int_0^t \frac{1}{D} g(s) e^{-\int_0^s \frac{1}{D} g(u)^2 du} ds \right], \quad (\text{Equation 20})$$

where,

$$C_0 = q(0) \frac{\left( 1 - e^{-\frac{1}{D} \int_0^{T_0} g(s)^2 ds} \right)}{\int_0^{T_0} \frac{1}{D} g(s) e^{-\int_0^s \frac{1}{D} g(u)^2 du} ds} \quad (\text{Equation 21})$$

and  $g(t) = \|F(x(t))\|_2$ . More details can be seen in next section. By combining two approaches we can calculate the potential landscape of the neural dynamics of *C. elegans*.

### The landscape construction for limit cycle system

When applying the original Gaussian-like approaches<sup>17</sup> to periodic oscillatory systems, we face a challenge where the covariance matrix may diverge to infinity. Hence, a novel and efficient method is required for computing the landscape of such periodic oscillatory systems. To approximate the solution of the Fokker-Planck equation, we introduce a novel method designed specifically for calculating the landscape of limit cycles. First, let's provide a restatement of the methods for calculating the landscape of multistable systems and attempt to explain the reason for the divergence issue. When we reorder  $\Sigma(x(t))$  to a vector  $\sigma(t)$ , the equation for solving the covariance can be reformulated as follows:

$$\frac{d\sigma(t)}{dt} = (I \otimes A + A \otimes I)\sigma(t) + 2D \cdot \text{vec}(I). \quad (\text{Equation 22})$$

This reveals that the evolution equation for covariance is essentially a linear ordinary differential equation. As the system's state, represented by  $x(t)$ , eventually approaches an attractor  $x^*$ , it's observed that around this attractor:  $v^T A(x^*) v < 0$  holds for all vector  $v \in \mathbb{R}^d$ . Consequently, the steady covariance matrix  $\sigma_1$  can be formulated as:

$$(I \otimes A(x^*) + A(x^*) \otimes I)\sigma_1 + 2D \cdot \text{vec}(I) = 0.$$

Under certain conditions, if  $v^T A(x^*) v < 0$  holds for all vectors  $v \in \mathbb{R}^d$ , it follows that  $v^T (I \otimes A(x^*) + A(x^*) \otimes I) v < 0$  holds for all vectors  $v \in \mathbb{R}^d$ . This means that the evolution matrix  $(I \otimes A(x^*) + A(x^*) \otimes I)$  is non-singular, and all its eigenvalues are negative. These properties ensure the convergence of the covariance equations described in Equation 22. However, when these approaches are employed for limit cycles, these properties can potentially break down, leading to the divergence issue observed in the iteration methods. In a periodic oscillatory system, as  $x(t)$  approaches a limit cycle, it becomes almost periodic with a period  $T_0$ . Consequently, Equation 22 can be reformulated into the following equation:

$$\frac{d\sigma(t)}{dt} = C(t)\sigma(t) + 2D \cdot \text{vec}(I),$$

where  $C(t)$  is defined as:

$$C(t) = I \otimes A(x(t)) + A(x(t)) \otimes I \quad (\text{Equation 23})$$

This equation is subject to the boundary condition:

$$\sigma(T_0) = \sigma(0). \quad (\text{Equation 24})$$

The numerical solution for Equation 23 can be expressed as:

$$\sigma(0) = \sigma(T_0) = B\sigma(0) + b_0, \quad (\text{Equation 25})$$

where  $B$  is computed as:

$$B = \lim_{n \rightarrow +\infty} \prod_{i=1}^n \left[ I + \frac{T_0}{n} C\left(\frac{n-i}{n}T_0\right) \right], \quad (\text{Equation 26})$$

and  $b_0$  is calculated as:

$$b_0 = 2D \lim_{n \rightarrow +\infty} \sum_{k=1}^n \prod_{i=1}^{n-k} \left[ I + \frac{T_0}{n} C\left(\frac{n-i}{n}T_0\right) \right] \cdot \text{vec}(I).$$

Therefore, the steady correlation can be determined by Equation 25, i.e.,

$$(I - B)\sigma(0) = b_0,$$

if the solution exists and is feasible. However, when dealing with a limit cycle instead of an attractor, it's possible that  $v^T A v$  is non-negative for the limit cycle direction  $v$ , and the eigenvalue of  $A + A^T$  may also be non-negative. Consequently, the matrix  $B$  in Equation 26 can become singular, and the solution may become infeasible. This is where the limitation of the iteration methods comes into play. From a global perspective, this limitation arises from the fact that the original hypothesis - that a Gaussian-like distribution will maintain its Gaussian shape in a moving local area - does not hold in this context. Instead, the origin Gaussian-like distribution will gradually fill the entire limit cycle. Therefore, the introduction of the novel method is necessary to address this issue. We start by assuming that around the limit cycle, the steady probability can be approximated as a low-rank Gaussian distribution in the orthogonal space to the tangent direction (the direction of  $F(x)$ ). This distribution is characterized by two functions:  $q(x)$  and  $\Sigma(x)$ . The probability density function  $p(x)$  is defined as follows:

$$p(x) = \frac{\int_C q(z) \frac{1}{(2\pi)^{d/2}} e^{-\frac{1}{2}(x-z)^T \Sigma(z)^{-1} (x-z)} dz}{\int_C q(z) \sqrt{\det \Sigma(z)} dz}, \quad (\text{Equation 27})$$

Here,  $C$  represents the limit cycle,  $q(x)$  and  $\Sigma(x)$  are functions for  $x$ , and the following paragraphs will show how to calculate them. We assume that in the steady state, there exists a local neighborhood where the flux (including Gaussian noise) entering or leaving maintains a balance at any point on the boundary of this neighborhood. As a result, the correlation matrix of the low-rank part (excluding the direction of  $F(x)$ ) can be obtained through a similar procedure as original approaches<sup>17,32</sup> by excluding the direction of  $F(x)$  from the matrix. Let's

denote  $v_1 = \frac{F(x)}{\|F(x)\|_2}$  as the unit vector in the tangent direction, and  $v_1, \dots, v_n$  as an orthonormal basis. We define a matrix  $Q$  as  $Q = (v_2, \dots, v_n)$ . The correlation matrix for  $v_2, \dots, v_n$ , denoted as  $\widehat{\Sigma} \in \mathbb{R}^{(d-1) \times (d-1)}$ , can be calculated through the equation:

$$\widehat{\Sigma} Q^T A^T Q + Q^T A Q \widehat{\Sigma} + Q^T D Q = 0. \quad (\text{Equation 28})$$

The solution can be obtained by:

$$\text{vec}(\widehat{\Sigma}) = -2D(I \otimes Q^T A Q + Q^T A Q \otimes I)^{-1} \text{vec}(I). \quad (\text{Equation 29})$$

Then the perpendicular part of  $\Sigma$  is given by  $Q \widehat{\Sigma} Q^T$ . Also, we find that the tangent part of  $\Sigma$  does not affect the final distribution around the limit cycle significantly, as it can be influenced by the density  $q(x)$ . Therefore, a fixed term is chosen as the tangent part:

$$\Sigma = Q \widehat{\Sigma} Q^T + d_0 v_1 v_1^T, \quad (\text{Equation 30})$$

Here,  $d_0$  is a small coefficient, usually taken as the diffusion coefficient  $D$ . Let's continue with the calculation of the density  $q(x)$  by restricting the Fokker-Planck equation to the limit cycle, which is essentially a one-dimensional manifold. The equation for this density can be formulated as follows:

$$\nabla(F(x)q(x) - D\nabla q(x)) = 0. \quad (\text{Equation 31})$$

Since  $x(t)$  is one-dimension, this is equivalent to,

$$F(x)q(x) - D\nabla q(x) = C_0,$$

$$\frac{dq}{dx} = \frac{1}{D} \left( F(x) \cdot \frac{\frac{dx}{dt}}{\left\| \frac{dx}{dt} \right\|_2} \cdot q(x) - C_0 \right).$$

With the properties of the limit cycle, we have,

$$\frac{dq}{dx} = \frac{1}{D} (\|F(x)\|_2 \cdot q(x) - C_0).$$

Let  $C = \{x(t) : t \in [0, T_0]\}$  be the limit cycle such that  $\frac{dx}{dt} = F(x)$ , and note  $g(t) = \|F(x(t))\|_2$ . We have,

$$\frac{dq}{dt} = \frac{dx}{dt} \cdot \frac{1}{D} (g(t) \cdot q - C_0),$$

$$\frac{dq}{dt} = \frac{g(t)^2}{D} q - C_0 \frac{g(t)}{D},$$

$$q(t) = e^{\frac{1}{D} \int_0^t g(s)^2 ds} \left[ q(0) - C_0 \int_0^t \frac{1}{D} g(s) e^{-\int_0^s \frac{1}{D} g(u)^2 du} ds \right].$$

Since  $q(0) = q(T_0)$ , we have,

$$q(0) = e^{\frac{1}{D} \int_0^{T_0} g(s)^2 ds} \left[ q(0) - C_0 \int_0^{T_0} \frac{1}{D} g(s) e^{-\int_0^s \frac{1}{D} g(u)^2 du} ds \right].$$

Since replacing  $q(x)$  by  $C_2 q(x)$  for any  $C_2 \in (0, +\infty)$  results the same final distribution  $p(x)$ , we can take  $q(0) = 1$ , and immediately have,

$$C_0 \int_0^{T_0} \frac{1}{D} g(s) e^{-\int_0^s \frac{1}{D} g(u)^2 du} ds = \left( 1 - e^{-\frac{1}{D} \int_0^{T_0} g(s)^2 ds} \right),$$

$$C_0 = \frac{\left( 1 - e^{-\frac{1}{D} \int_0^{T_0} g(s)^2 ds} \right)}{\int_0^{T_0} \frac{1}{D} g(s) e^{-\int_0^s \frac{1}{D} g(u)^2 du} ds}.$$

Finally, the density function  $q(t)$  can be calculated by,

$$q(t) = e^{\frac{1}{D} \int_0^t g(s)^2 ds} \left[ q(0) - C_0 \int_0^t \frac{1}{D} g(s) e^{-\int_0^s \frac{1}{D} g(u)^2 du} ds \right]. \quad (\text{Equation 32})$$

### QUANTIFICATION AND STATISTICAL ANALYSIS

Statistical analysis was performed using MATLAB version R2020b, unless mentioned otherwise.